Improved lattice spectroscopy of minimal walking technicolor

PHYSICAL REVIEW D **84,** 034506 (2011)

Improved lattice spectroscopy of minimal walking technicolor

Francis Bursa[*]
Jesus College, University of Cambridge, Cambridge, England

Luigi Del Debbio[†]
SUPA, School of Physics and Astronomy, University of Edinburgh, Edinburgh, Scotland

David Henty[‡]
EPCC, University of Edinburgh, Edinburgh, Scotland

Eoin Kerrane[§]
SUPA, School of Physics and Astronomy, University of Edinburgh, Edinburgh, Scotland

Biagio Lucini[‖]
College of Science, Swansea University, Swansea, Wales

Agostino Patella[¶]
CERN, Geneva, Switzerland

Claudio Pica[**]
CP^3-Origins & IMADA, University of Southern Denmark, Odense, Denmark

Thomas Pickup[††]
Rudolf Peierls Centre for Theoretical Physics, University of Oxford, Oxford, England

Antonio Rago[‡‡]
Department of Physics, Bergische Universität Wuppertal, Wuppertal, Germany
(Received 30 April 2011; published 26 August 2011)

We present a numerical study of spectroscopic observables in the SU(2) gauge theory with two adjoint fermions using improved source and sink operators. We compare in detail our improved results with previous determinations of masses that used point sources and sinks and we investigate possible systematic effects in both cases. Such comparison enables us to clearly assess the impact of a short temporal extent on the physical picture, and to investigate some effects due to the finite spatial box. While confirming the IR-conformal behavior of the theory, our investigation shows that in order to make firm quantitative predictions, a better handle on finite size effects is needed.

DOI: 10.1103/PhysRevD.84.034506 PACS numbers: 11.15.Ha, 12.60.Nz

I. INTRODUCTION

A new strongly interacting theory [1,2] with an approximate [3–5] or exact [6] infrared (IR) fixed point is an appealing possibility for explaining electroweak symmetry breaking. This framework, known as Technicolor, has been reviewed recently in, e.g., [7–9]. Technicolor theories are inherently nonperturbative and therefore require adequate tools to study their strong dynamics. Theories with conformal or near-conformal dynamics can be exposed in the context of the gauge-string duality [10,11]. However, in addition to the wanted fermion and gauge boson degrees of freedom, field theory duals of string theories in general contain extra scalar fields. A possible *ab initio* approach relies on numerical simulations of candidate Technicolor theories discretized on a spacetime lattice (see, e.g., [12,13] for recent reviews).

One could generate an infrared fixed point in a gauge theory by adding a low number of fermion flavors in higher gauge representations to a gauge theory with a low number of colors. The minimal vectorlike gauge theory with this property, termed minimal walking technicolor (MWT), has gauge group SU(2) and two flavors of Dirac fermions in the adjoint representation [14]. Some recent lattice studies of MWT [15–17] have attempted to identify a near-conformal behavior directly from the behavior of the coupling and anomalous dimensions of the theory under renormalization group flow. Others, including this work, perform

[*]f.bursa@damtp.cam.ac.uk
[†]luigi.del.debbio@ed.ac.uk
[‡]d.henty@epcc.ed.ac.uk
[§]eoin.kerrane@ed.ac.uk
[‖]b.lucini@swansea.ac.uk
[¶]agostino.patella@cern.ch
[**]pica@cp3.sdu.dk
[††]pickup@thphys.ox.ac.uk
[‡‡]rago@physik.uni-wuppertal.de

measurements of physical observables in the theory and attempt to identify signals of near-conformal dynamics from their behavior [18–25]. All the evidence accumulated so far for this theory favors a conformal or near-conformal scenario and seems to exclude standard confinement and chiral symmetry breaking behavior. However, more systematic studies need to be performed before the IR properties of the theory can be determined with confidence.

MWT with a nonzero fermion mass and defined in a finite volume, as simulated for practical reasons on the lattice, cannot be conformal. If the chiral continuum theory possesses an infrared fixed point, the lattice results will be described by a mass-deformed conformal gauge theory [22,24–29]. In approaching a conformal limit, the theory respects the hyperscaling property, whereby all spectral masses M in the theory scale identically. They must vanish in the limit of vanishing fermion mass m. If the IR fixed point is approximate, the theory displays conformal behavior for an intermediate range of masses m and crosses over to the confining and chiral symmetry breaking behavior in the chiral limit.

The standard way to extract masses from lattice simulations is to look at the exponential decay of correlators of operators with the quantum numbers of interest. For infinite separation between the source and sink operator, the exponential decay is governed by the ground state mass in the channel being explored. At finite time extent, this leading behavior receives corrections that are exponentially suppressed in the mass difference between the ground state and the excitations. Underestimating the importance of these corrections leads to systematic errors in the determination of the ground state mass. In addition to the effects of the finite maximal separation between the source and the sink (often referred to as finite temperature effects), the finite spatial extension of the lattice can also give sizeable corrections to the spectral masses.

The simplest source and sink observables to study for mesons are fermion bilinears in which the two fermion fields are at the same lattice point (*point sources*). These sources have been widely used in previous investigations of the spectrum of MWT. However, the experience accumulated over 30 years of numerical studies in lattice QCD favors the use of *extended sources*, which are gauge-invariant combinations of two fermion fields at different points, engineered for reducing the contamination from the excited states. In lattice QCD, masses extracted from correlators of extended sources prove to be affected by smaller systematic errors. In this paper, we investigate whether this proves to be the case also for MWT. Specifically, we perform a study of mesonic observables extracted from extended sources using the configurations presented in [19,22,25]. We explore a large set of schemes for building extended operators and we systematically analyze their efficiency for the computation of meson masses and decay constants, comparing the results with results obtained using point sources. With this study, we expect to determine the size of systematic uncertainties in current studies, which have as yet been largely unexplored, and to assess their impact on the physical picture emerging from the previous spectroscopical studies. Some of the results presented here have already appeared in Ref. [30].

The rest of the paper is organized as follows. In Sec. II we describe the background to this study and briefly illustrate the effects of the use of different smearings on effective observables. Technical details on the smearing procedures and the resulting observables can be found in Appendices A and B, respectively. In Sec. III we quantify the consequences of the smearing both for autocorrelation times and quality of plateaux. A full set of results obtained using wall smearing are presented in Sec. IV, while in Sec. V we comment on the significant finite-volume effects highlighted by the smeared results. Appendices C and D list the numerical values of the quantities studied in this work. Finally, our conclusions are reported in Sec. VI. Tables I–X in Appendix C and Tables XI–XVIII in Appendix D list the numerical values of the quantities studied in this work.

II. SYSTEMATIC SPECTROSCOPY

This study builds on the work described in [19,25] where spectroscopic observables of MWT were measured through lattice simulations. The computation was performed using the HIREP code, designed to simulate theories of a generic number of colors, and with fermions in a generic representation of the gauge group. The simulations used the Wilson gauge action and the Wilson fermion formulation along with the RHMC algorithm. A number of lattice volumes have been analyzed, from 16×8^3 to 64×24^3 with a range of bare quark masses. The majority of the ensembles have been generated at $\beta = 2.25$, although we do here present the results of some additional runs on the largest lattice at $\beta = 2.1$.

For this study we have performed some alternative analyses to those in [25]. The CHROMA suite of lattice software [31] has been extended to operate with several fermionic representations other than the fundamental, including the adjoint. This will allow us to utilize the in-built smearing routines of CHROMA for our spectroscopic study.

In order to test the modified CHROMA, we measured the local correlators as defined in (A3), with $\Gamma = \Gamma'$ both with HIREP $[f_\Gamma^{(h)}(t)]$ and CHROMA $[f_\Gamma^{(c)}(t)]$. We used an ensemble of configurations on a 8×4^3 lattice with $\beta = 2.25$ and fermion bare mass $am_0 = -1$. Figure 1 illustrates the discrepancy between the two determinations, defined as

$$D_1 = \sqrt{\sum_t (f_\Gamma^{(c)}(t) - f_\Gamma^{(h)}(t))^2} \quad D_2 = \sqrt{\sum_t \left(\frac{f_\Gamma^{(c)}(t) - f_\Gamma^{(h)}(t)}{f_\Gamma^{(h)}(t)}\right)^2}. \tag{2.1}$$

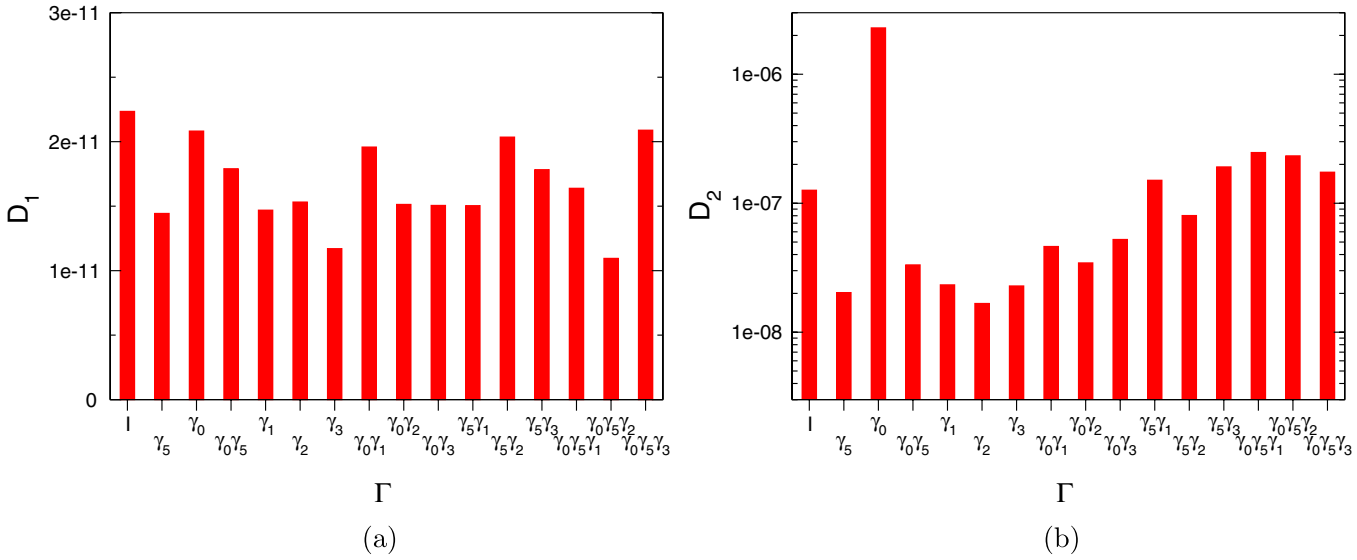

FIG. 1 (color online). Discrepancies between local correlators from HIREP and CHROMA, computed to test the extension of CHROMA (for working with adjoint fermions) against HIREP.The quantities D_1 and D_2 defined in (2.1) are shown in Figs. 1(a) and 1(b), respectively.

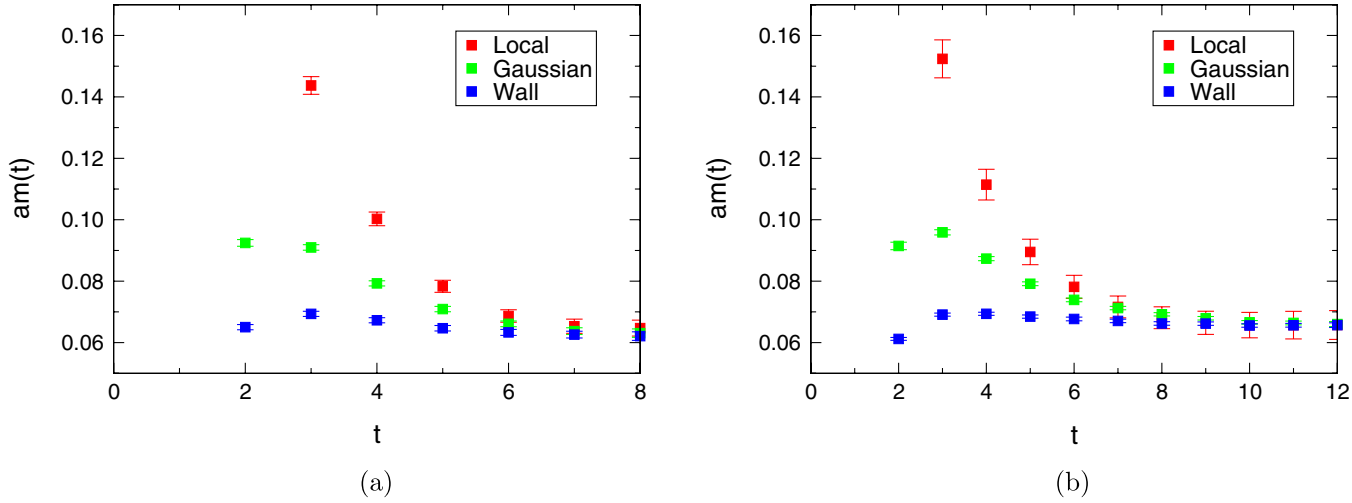

FIG. 2 (color online). Comparison of the PCAC mass from different smearings at $am_0 = -1.175$ on a 16×8^3 [Fig. 2(a)] and a 24×12^3 lattice [Fig. 2(b)].

We proceeded to utilize the in-built smearing routines found in CHROMA to perform measurements on the gauge configurations generated with HIREP using a number of different quark smearings. We have investigated the use of both wall smearing and a gauge-invariant Gaussian smearing, as defined in Appendix A 2. Definitions of all observables discusses can be found in Appendix B.

Gaussian smearing involves two parameters, which can be chosen to optimize the technique. They are the width of the smearing function and the number of applications of the smearing operator, which must be large enough to reasonably approximate the Gaussian form. These two parameters have been adjusted in order to maximize the overlap of the smeared operator with the ground state. On the other hand, the wall smearing is a parameter-free procedure.

We systematically compared local, Gaussian (with optimized parameters) and wall-smeared sources on our ensembles. At our lightest masses, the wall-smeared sources have the largest overlap with the ground state, which is reflected in the flattest effective masses. In Figs. 2–4 we show, respectively, the partially conserved axial current (PCAC) and pseudoscalar (PS) effective masses and the PS effective decay constant computed with the three methods.

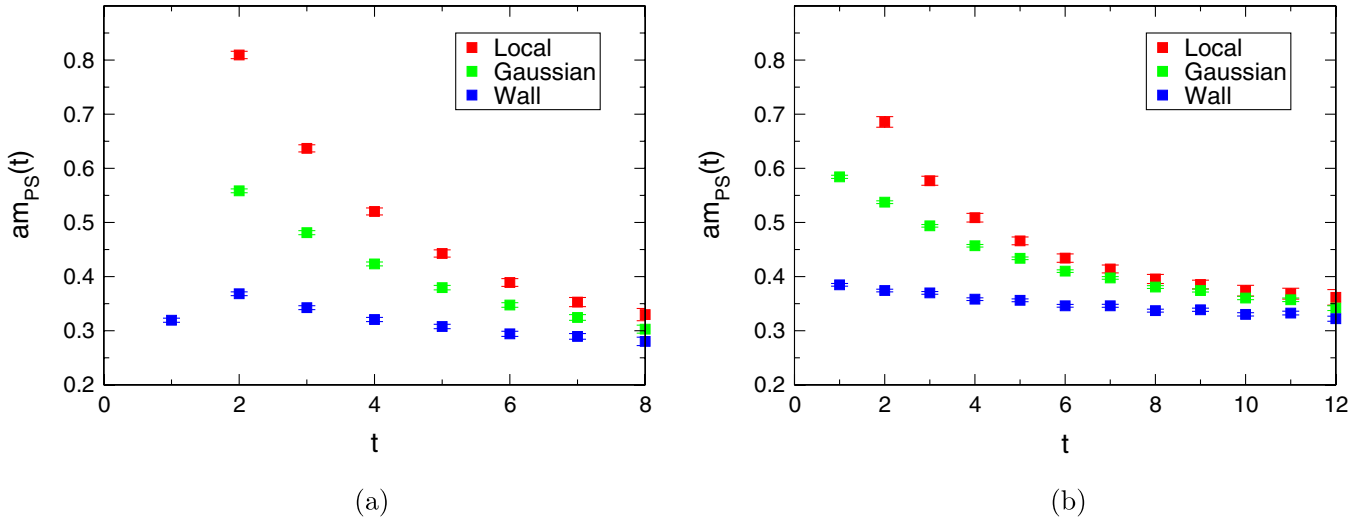

FIG. 3 (color online). Comparison of the pseudoscalar mass from different smearings at $am_0 = -1.175$ on a 16×8^3 (Fig. 3(a)) and a 24×12^3 lattice (Fig. 3(b)).

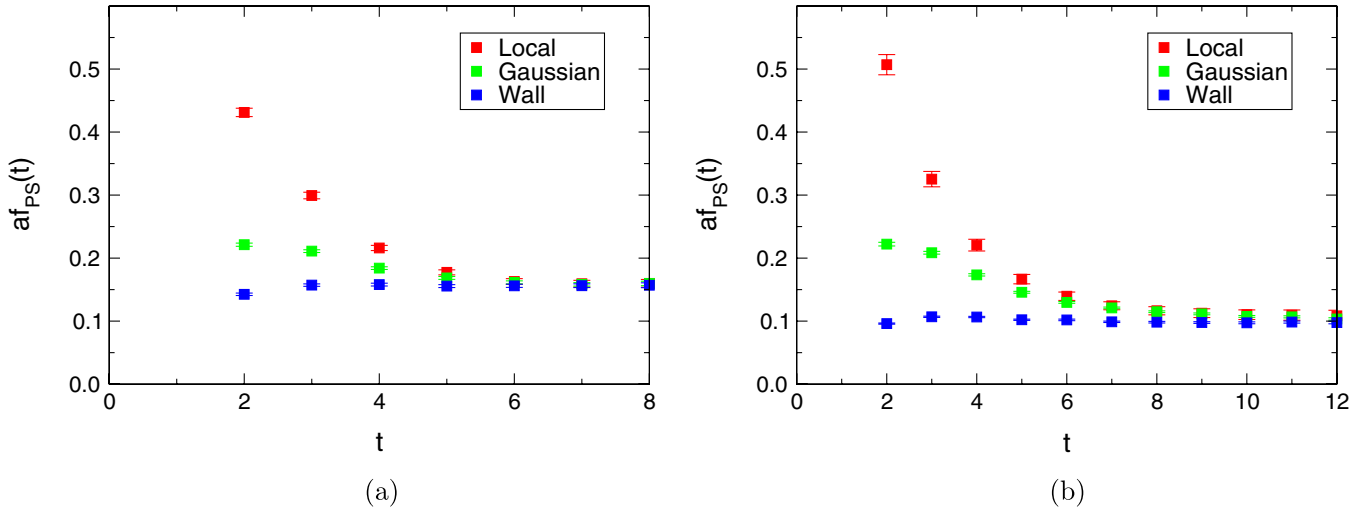

FIG. 4 (color online). Comparison of the pseudoscalar decay constant from different smearings at $am_0 = -1.175$ on a 16×8^3 (Fig. 4(a)) and a 24×12^3 lattice (Fig. 4(b)).

Since we are mainly interested in the light masses, we will focus on the wall-smeared results in the rest of this work.

III. EFFECTIVENESS OF THE WALL-SMEARED SOURCES

Using smeared sources allows us to choose an operator with a larger projection onto the ground state of a given channel. The wave function of the ground state is spread over many lattice sites, and we can improve the overlap of the operator with the ground state by giving a spatial size to the source. The smeared correlator will be less contaminated by the excited states, and therefore it will be characterized by a single cosh signal for a larger temporal separation than the one constructed with point operators. This is reflected in a longer plateau in the effective mass. On the contrary one drawback of using smeared sources is that it makes the analysis more sensitive to the algorithm's autocorrelation time. In this section we propose a quantitative study of these two aspects: the behavior of the size of the plateaux for different kinds of sources, and the autocorrelation time connected with the use of these sources.

A. Autocorrelations

Correlators generated using sources with an extended spatial profile are expected to be associated with longer autocorrelation times, due to the fact that the low energy modes of the fields need more Monte-Carlo time to propagate. This effect is observed throughout our study, indeed the autocorrelation time associated with the results from

smeared correlators is generically at least of the order of twice that of those involved with the local correlators. This is supported both by the direct measurement of the integrated autocorrelation time [32] associated with the observables, and by the analysis of the behavior of the standard deviation of the observables.

Both the aforementioned studies have been performed by grouping the N data into N/b blocks of a given length b. A reduced data set of length N/b is created by averaging the required statistic over each block. A bootstrap analysis is then performed on the reduced data set. By increasing the block size b, we are creating effective estimates less and less autocorrelated, hence when the block size is bigger than the autocorrelation we expect to see a plateau appearing in the standard deviation, signaling that the reduced data set is decorrelated. We observe that the plateau starts at a block size corresponding to an integrated autocorrelation time of order 1.

Our analysis of the autocorrelation is illustrated in Fig. 5, for the PS effective mass obtained with both local (L), and wall-smeared (W) sources, evaluated at two temporal points.

From the left panel of Fig. 5 we see that the measured autocorrelation time for the smeared results are generically larger than those for the local results. From the right panel of Fig. 5 we see that the standard deviation of our observable increases for both sets of correlators as we increase the block size from zero, up to a point where it appears to reach a plateau for a significant range of b for both cases. The value of b where this plateau sets in is interpreted as the length in simulation time over which the data are uncorrelated. From the right panel of Fig. 5 we would conclude that the autocorrelation time of our local result was ~ 30 while that of the smeared result was ~ 80. Indeed returning to the left panel of Fig. 5 we see that at this value of b, the corresponding value of the integrated autocorrelation time is close to 1, which supports our conclusion.

This picture is replicated across our ensembles, and we have accounted for this in our results by conducting our bootstrap analysis over appropriately reduced data sets.

B. Plateaux of the effective masses

If the smearing procedure is effectively suppressing the contribution of the excited states to the correlators, one has to observe the effective masses flattening around the midpoint $t = L_t/2$, and the plateaux becoming longer when visible. We can quantitatively estimate the flatness of the effective mass using the absolute value of the incremental ratio of the effective mass between $t = L_t/2$ and $t = L_t/2 - \Delta t$:

$$\frac{\Delta m_{\mathrm{PS}}}{\Delta t} \equiv \left| \frac{m_{\mathrm{PS}}(L_t/2 - \Delta t) - m_{\mathrm{PS}}(L_t/2)}{\Delta t} \right|. \tag{3.1}$$

A value for $\Delta m_{\mathrm{PS}}/\Delta t$ compatible with zero implies that the plateau in the effective mass is at least Δt points long. For very small values of Δt the incremental ratio is dominated by the statistical error. On the other hand the effective masses obtained with smeared sources are sometimes nonmonotonic. In this case the incremental ratio defined with a too large value for Δt is not a good estimate for the flatness of the plateau. An intermediate range of values for Δt exists, in which our analysis makes sense. We explicitly checked that our conclusions do not change choosing Δt in such a range, and we chose $\Delta t = 4$ for definiteness.

In general the smaller $\Delta m_{\mathrm{PS}}/\Delta t$ is, the flatter the plateau. Notice that it is important to take the absolute value

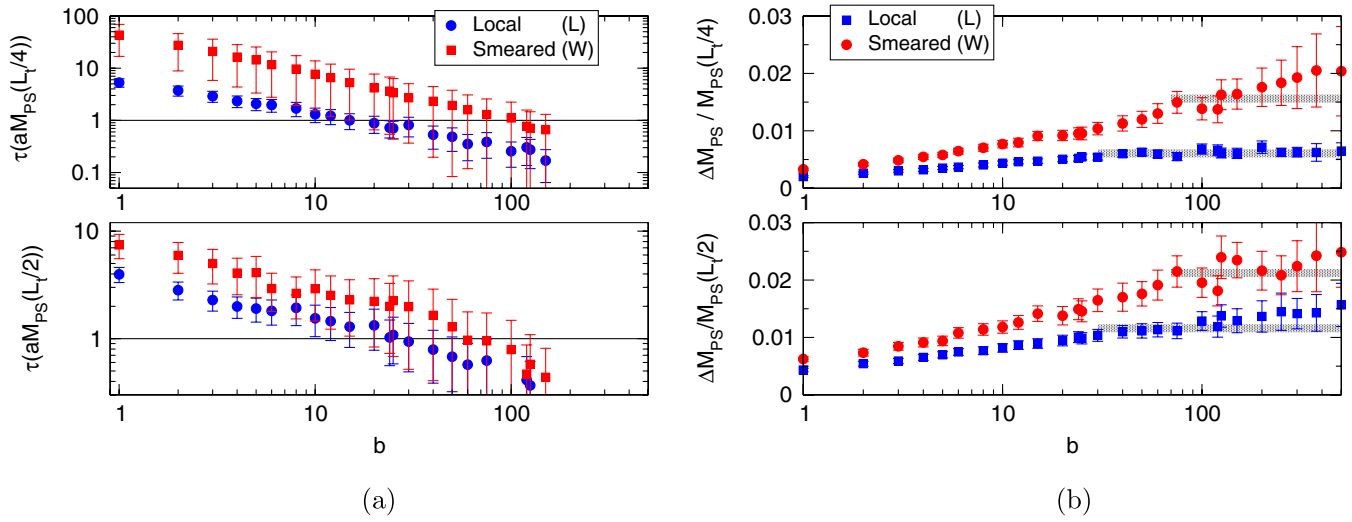

FIG. 5 (color online). Autocorrelation analysis conducted on a 24×12^3 lattice at $am_0 = -1.175$, for the PS effective mass in two temporal points.Figure 5(a) shows the integrated autocorrelation time as a function of the block size b. Figure 5(b) shows the relative error as a function of the block size b. The plateaux of the relative error are highlighted with shadowed rectangles. The plateaux in the relative error set in when the integrated autocorrelation time becomes of order 1.

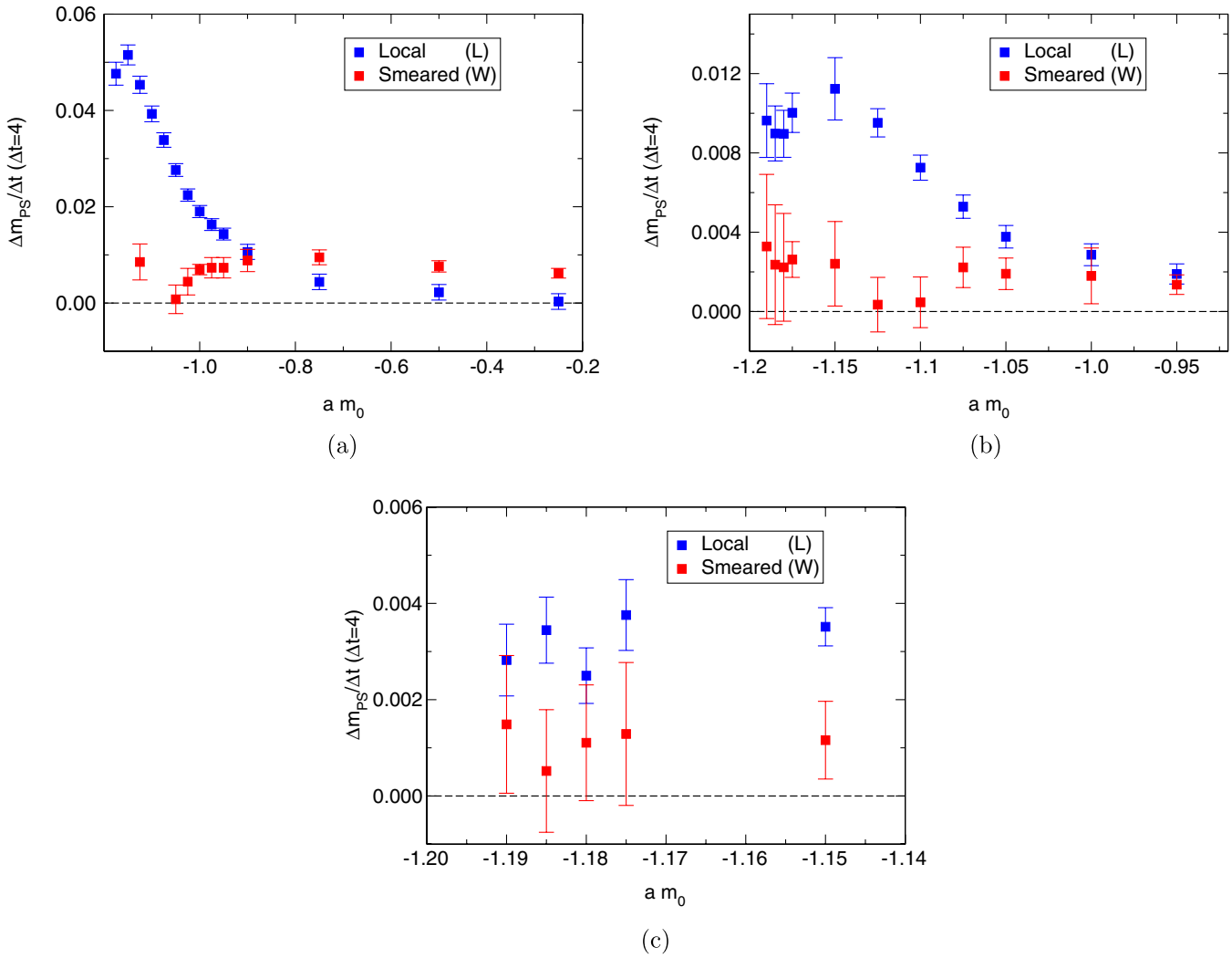

FIG. 6 (color online). Incremental ratio $\Delta m_{\mathrm{PS}}/\Delta t$ as a function of the bare mass. The smaller this quantity, the better the quality of the plateau of the PS effective mass. On the (a) 16×8^3 lattice, the local correlators give flatter plateaux for bare masses larger than -0.8, while the smearing is effective below -0.9. On the (b) 24×12^3 lattice, the local and smeared sources give plateaux of similar quality for the two heaviest masses, while the smearing is effective for all the other masses. Finally, the smearing is always effective on the (c) 32×16^3 lattice.

in the definition above: while the effective mass defined from local correlators is always decreasing, it is not so for smeared correlators.

In Fig. 6, the quantity $\Delta m_{\mathrm{PS}}/\Delta t$ is plotted for all our pseudoscalar effective masses on the 16×8^3, 24×12^3, and 32×16^3 lattices, both for local and wall-smeared correlators.

One expects that at small masses the wave function of the pseudoscalar meson is more spread, hence the wall-smeared source should have a larger overlap with the ground state. On the contrary at large masses the wave function is more localized, therefore, the local sources should work better. Our analysis presented in Fig. 6 substantiates this expectation. On the 16×8^3 lattice the wall-smeared sources give better or comparable plateaux than the local sources for masses $am_0 \leq -0.9$. On the 24×12^3 and 32×16^3 lattices the wall-smeared sources are to be (sometimes marginally) preferred to the local ones for all the simulated masses.

In the presentation of the results obtained from wall-smeared sources we will always cut the masses in the 16×8^3 lattice for which the local sources are actually preferable to the wall-smeared ones, unless otherwise stated.

Finally, we point out that the same analyses using the effective V meson mass and the effective PS decay constant produce very similar results.

IV. RESULTS

In the present section, we will present our results for the mesonic observables from the wall-smeared sources. Complete results of all observables analyzed are also presented in Sec. III. Although only the results at $\beta = 2.25$

will be discussed in detail, measurements at $\beta = 2.1$ can also be found in the tables. For the full local results, the reader is referred to [25].

We will consider only those fermionic masses for which the wall-smeared sources give an improvement on the plateaux of the effective masses with respect to the local sources, as discussed in Sec. III B. For all these masses, the wall-smeared results have to be trusted more than the local ones. The disagreement between the two determinations gives an estimate of the systematic error due to a bad determination of the plateaux, mainly affecting our previous results obtained from the local sources.

In order to quantify this disagreement we use two different estimators: the *pull* and the *relative discrepancy*. We will denote $O_L \pm \Delta O_L$ and $O_S \pm \Delta O_S$ the determination of the generic observable O using, respectively, local and smeared sources. The pull estimates the relative size of the systematic and statistical errors and is defined as

$$P(O) = \frac{|O_L - O_S|}{\sqrt{\Delta O_L^2 + \Delta O_S^2}}. \tag{4.1}$$

A small value for the pull is desirable, indicating that the systematic errors are smaller than the statistical ones. However a small value for the pull can be obtained either with a small systematic error or with a large statistical one. Therefore, it is not an absolute estimator of the goodness of a measurement. The relative discrepancy estimates the systematic error, relative to the average of the two determinations:

$$D(O) = \frac{2|O_L - O_S|}{O_L + O_S}. \tag{4.2}$$

A small value for the relative discrepancy indicates that the systematic effects contribute to a small fraction of the determination of the observable O.

In what follows, we will consider separately the PCAC quark mass, the PS and V masses and their ratios, the PS and V decay constant. Again, we refer the reader to Appendix B for the definition of these observables. We will present the results for the wall-smearing sources, and we will discuss the differences with the local-source results using the pull and the relative discrepancy.

A. PCAC mass

In Fig. 7 results for the PCAC mass from the wall-smeared correlators on all $\beta = 2.25$ ensembles are presented. The inset illustrates a close up of the approach to the chiral limit, with a linear extrapolation to zero quark mass. Using this we find the critical bare quark mass to be $am_c = -1.2022(14)$, from a fit using the three lightest points on the 24×12^3 lattice, which compares very well to the result obtained from the local data [25].

In Fig. 8 we show the stability of this fit against varying the number of points used. We compare this to the result

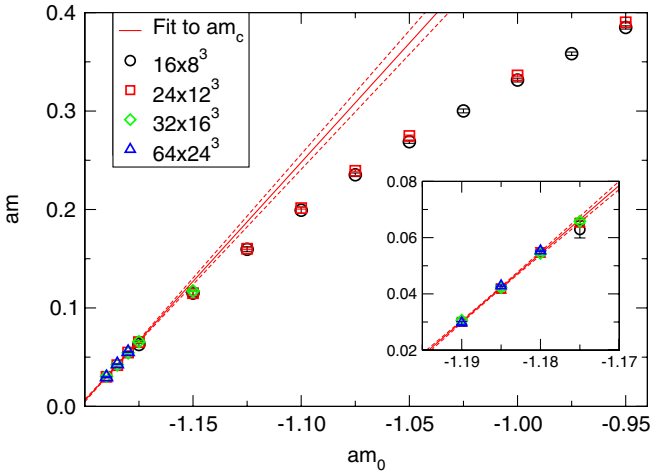

FIG. 7 (color online). PCAC quark mass for ensembles at $\beta = 2.25$, computed with wall-smeared sources, as a function of the quark bare mass. The result of the linear fit for extracting the critical bare mass is also shown. In the inset, the lightest masses are zoomed in.

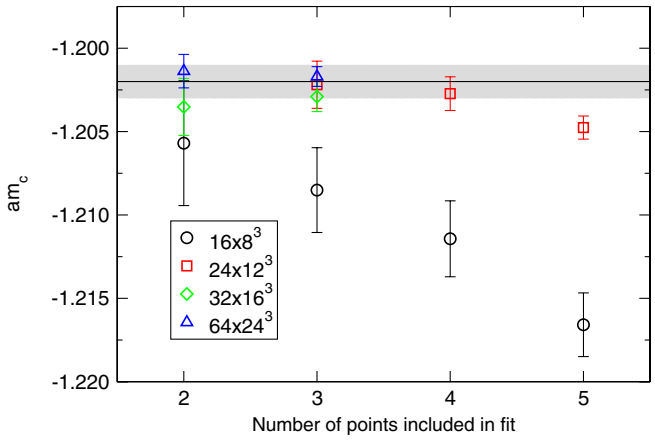

FIG. 8 (color online). Critical quark mass extracted from a linear fit with different fit ranges. The critical mass as obtained from local data is shown as a grey band.

obtained from local correlators, noting the agreement. It is also clear that finite-volume effects for this quantity are at most comparable with the statistical uncertainty.

In Fig. 9 we show the pull and the relative discrepancy as defined in Eqs. (4.1) and (4.2) between the local and wall-smeared determinations of the PCAC quark mass. We include all the masses at which the wall-smeared sources give an improvement of the plateaux in the effective masses over the local sources. As shown in the left panel of Fig. 9, the pull is always smaller than 1 (or marginally larger than 1 for the smallest volume), indicating that the systematic error due to a short temporal direction is of the order of the statistical uncertainty. The right panel of Fig. 9 shows that the systematic error is of order of a few percents for the PCAC mass.

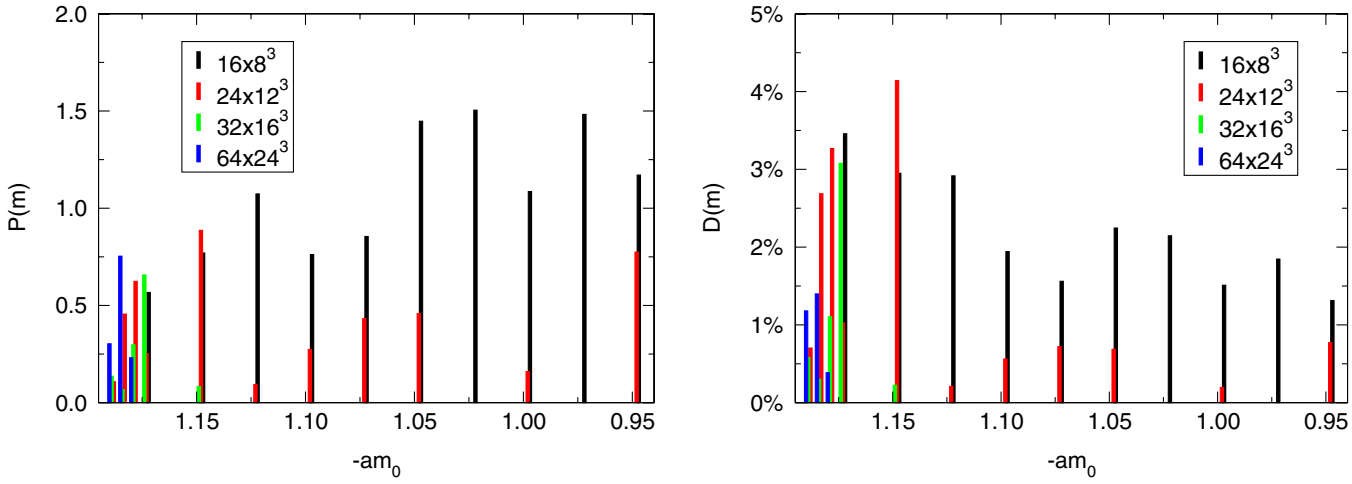

FIG. 9 (color online). Pull and relative discrepancy as defined in Eqs. (4.1) and (4.2) for the PCAC quark mass ($\beta = 2.25$).

B. Meson masses

Figure 10 shows the results obtained for the pseudoscalar mass $M_{\rm PS}$ as a function of the PCAC quark mass m, from the $\beta = 2.25$ data. Figure 11 shows the ratio $M_{\rm V}/M_{\rm PS}$. We recall that the existence of a plateau at small masses of this ratio was one of the main ingredients for arguing in favor of an IR fixed point in [22,25]. We notice that the smeared results stabilize the plateaux at very small masses (especially by smoothing the behavior of the largest volumes), while making more visible some finite-volume effects at intermediate masses. We will discuss the finite-volume effects in Sec. V.

We also report the pull and relative discrepancy as defined in Eqs. (4.1) and (4.2) between the local and wall-smeared determinations of the PS mass in Fig. 12. Again, we include all the masses at which the wall-smeared sources give an improvement of the plateaux in the effective masses over the local sources. The local and smeared sources give quite different results at small masses. The relative discrepancy has a very regular behavior: it is larger for lighter masses or smaller volumes. For bare masses below -1.15 one has to use lattices larger than the 24×12^3 in order to keep the relative discrepancy below the 10% level. Although the relative discrepancy can get fairly large at these masses, the pull is always below 3 which means that the two determinations are compatible within the 3σ range. This effect is generated by an increase of the relative statistical error at light masses.

Figure 13 shows the pull and relative discrepancy between the local and wall-smeared determinations of the $M_{\rm V}/M_{\rm PS}$ ratio. The situation is better here. The central values of the two determinations never differ by more

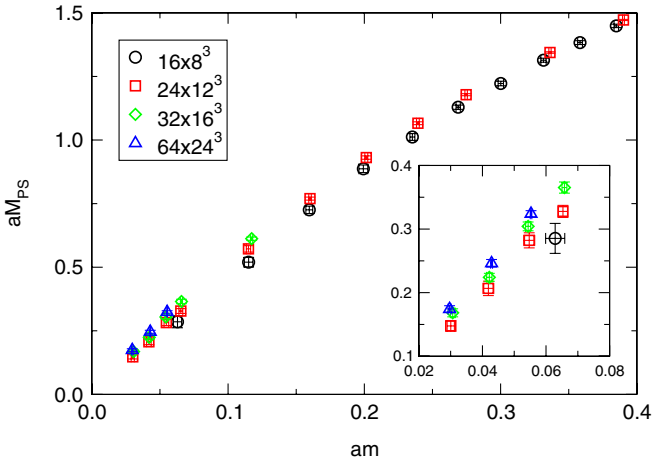

FIG. 10 (color online). Pseudoscalar meson mass for ensembles at $\beta = 2.25$, computed with wall-smeared sources, as a function of the PCAC mass. In the inset, the lightest masses are zoomed in.

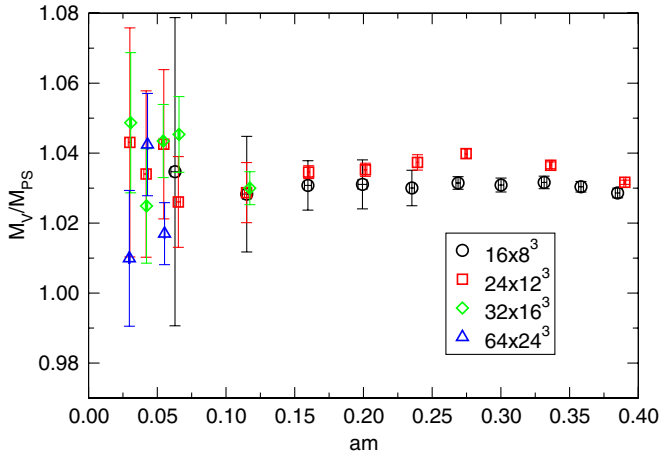

FIG. 11 (color online). Ratio of $M_{\rm V}$ to $M_{\rm PS}$ for ensembles at $\beta = 2.25$, computed with wall-smeared sources, as a function of the PCAC mass. The plateau in this ratio at small masses has been interpreted in our previous works [22,25] as a signal for IR conformality. The smeared sources have amplified the finite-volume effects at masses around $am \simeq 0.3$. This effect will be discussed in Sec. V.

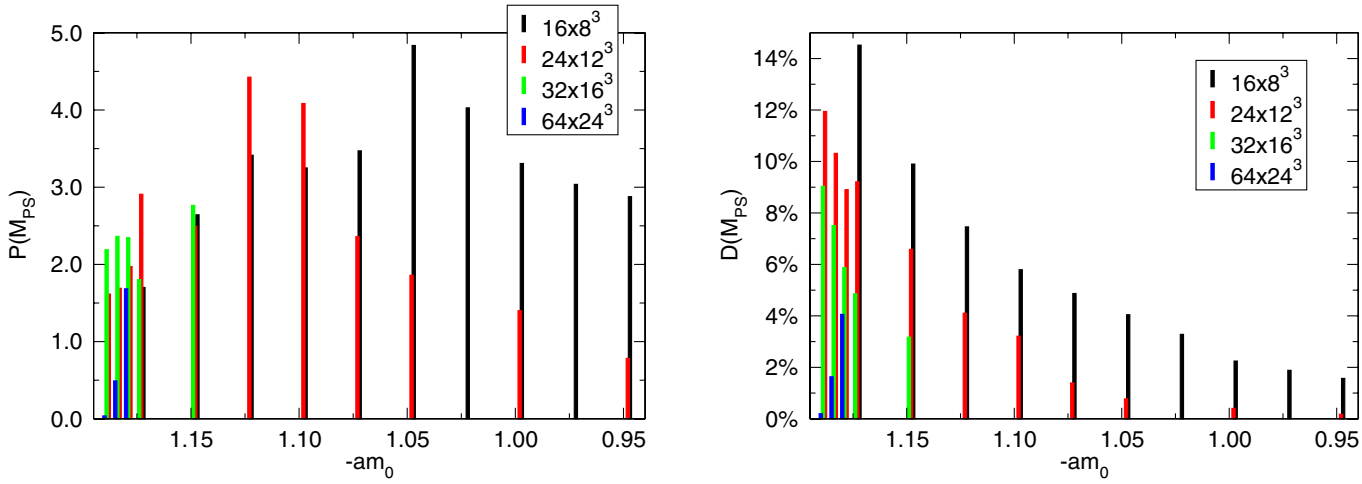

FIG. 12 (color online). Pull and relative discrepancy as defined in Eqs. (4.1) and (4.2) for the PS mass ($\beta = 2.25$).

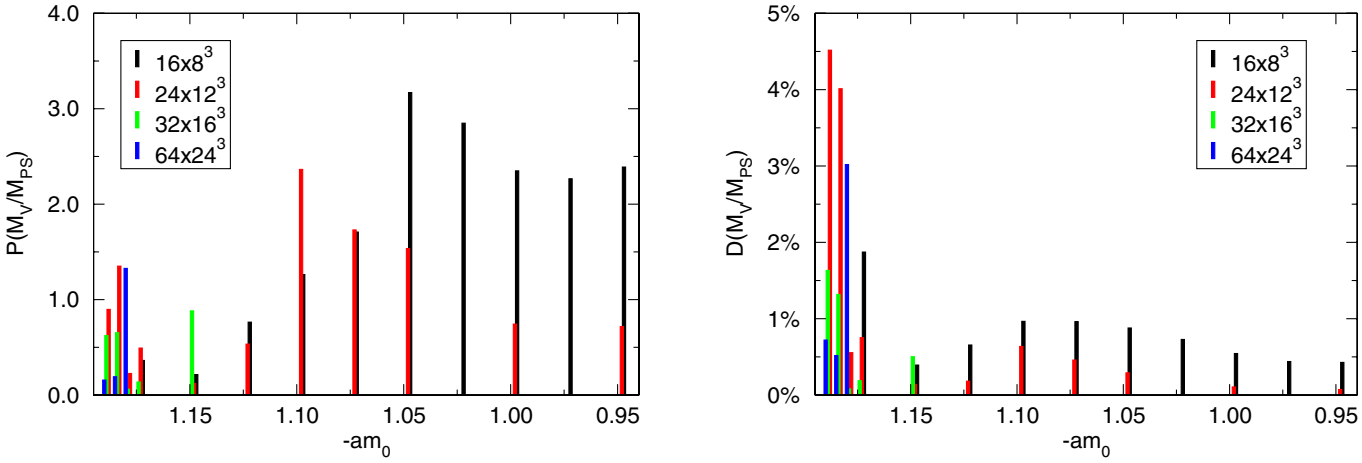

FIG. 13 (color online). Pull and relative discrepancy as defined in Eqs. (4.1) and (4.2) for the ratio of the V mass over the PS mass ($\beta = 2.25$).

than 5% (relative discrepancy), and they are generally compatible (except the smallest volume) within the 2σ range (pull).

C. Decay constants

Among the observables considered in this study, the PS decay constant is the quantity most affected by systematic errors due to a short temporal dimension. The relative discrepancy between the local and smeared determinations (Fig. 14) is almost always very large. On the 24×12^3, 32×16^3, and 64×24^3 lattices, this large relative discrepancy is partly compensated by a large statistical error. In most of the cases the two determinations are compatible (sometimes marginally) within 3σ of the statistical uncertainty (pull). On the 16×8^3 lattice, the difference is more dramatic. However for intermediate masses, the wall-smeared source gives a better defined plateau in the effective PS decay constant as discussed in Sec. III B, and therefore the smeared results have to be trusted more than the local ones.

Figure 15 shows the results for the PS decay constant from wall-smeared sources. The difference between the results on the 16×8^3 and 24×12^3 lattices are striking (and was absent in the local determination). This finite-volume effect will be discussed in Sec. V. We also show for completeness the ratio F_V/F_{PS} in Fig. 16.

V. COMMENTS ON FINITE-VOLUME EFFECTS

The wall-smeared results helped us to better understand how finite spatial volume affects the mesonic observables. In Fig. 17 we plot the PS and V masses, their ratio and PS decay constant on the 16×8^3 and 24×12^3 lattices for $am_0 = -1.05$ and $\beta = 2.25$, both from local and wall-smeared sources. For each observable, the gap between the two lattices becomes wider when wall-smeared sources are considered. Having only the data from local sources, one

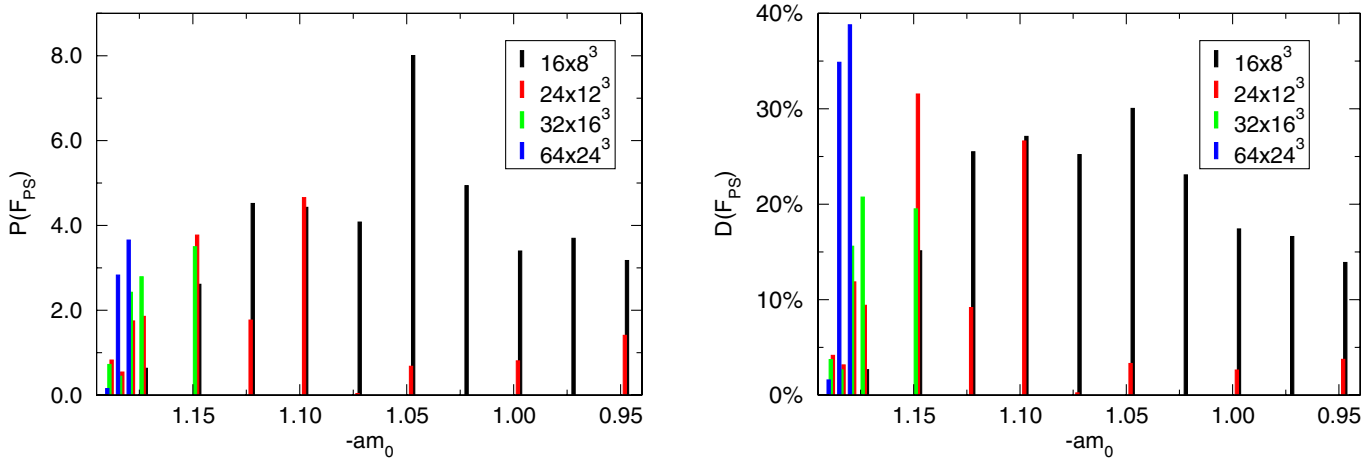

FIG. 14 (color online). Pull and relative discrepancy as defined in Eqs. (4.1) and (4.2) for the PS decay constant ($\beta = 2.25$).

can be tempted to underestimate the finite-volume errors. This would be a mistake: the mild dependence on the volume of the local data is actually given by a cancellation of two larger effects: the finite volume and the bad determination of the plateaux in the effective masses.

In order to clarify this point, it is useful to look directly at the effective PS mass (Fig. 18) and the effective PS decay constant (Fig. 19). We will comment on the effective PS mass, but all the observations will be equally valid for the effective PS decay constant.

The first observation is that the effective masses from local sources are always decreasing with the Euclidean time. Therefore, if the temporal size is not large enough to contain the plateau of the effective mass, the estimated mass will be larger than the real one. On the other hand the effective masses from wall-smeared sources for on this ensemble are increasing (although this is not true across all ensembles). Therefore, if the plateau is not reached, the estimated mass will be smaller than the real one.

Consider now the 24×12^3 effective masses in Fig. 18. The local and wall-smeared sources give effective masses whose quality in terms of flatness is similar [compare with Fig. 6(b)], and the plateau is not clearly visible in any of the effective masses. However, since the gap between the local and wall-smeared effective masses closes down in the midpoint $t = 12$, one can argue that the plateau is effectively reached there.

The situation is completely different for the 16×8^3. The gap between the local and wall-smeared effective masses is always quite big. The wall-smeared source gives a much flatter effective mass than the local source [compare with Fig. 6(a)]. In order to obtain a more precise estimate for the pseudoscalar mass on the spatial volume 8^3, we simulated on a 64×8^3 lattice. In this case the temporal extent is large enough to obtain very good plateaux for both the local and wall-smeared effective masses.

By comparing the effective masses on the 24×12^3 and 64×8^3 lattices it is clear that the finite volume has the

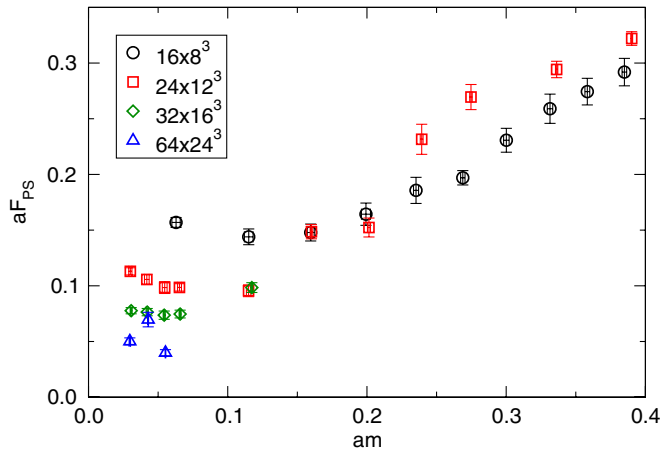

FIG. 15 (color online). Pseudoscalar decay constant for ensembles at $\beta = 2.25$, computed with wall-smeared sources, as a function of the PCAC mass.

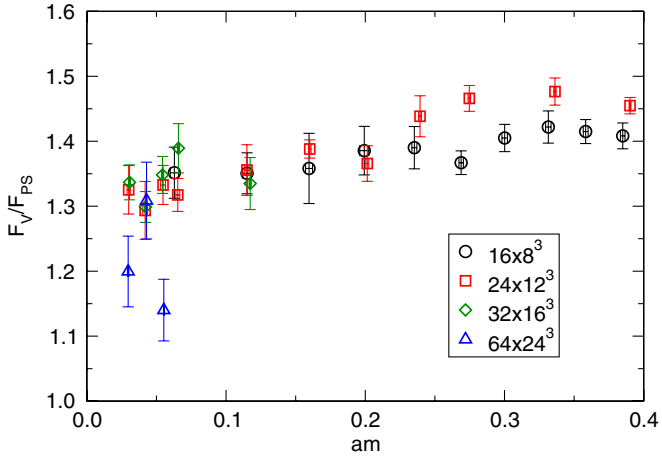

FIG. 16 (color online). Ratio of vector and pseudoscalar decay constants.

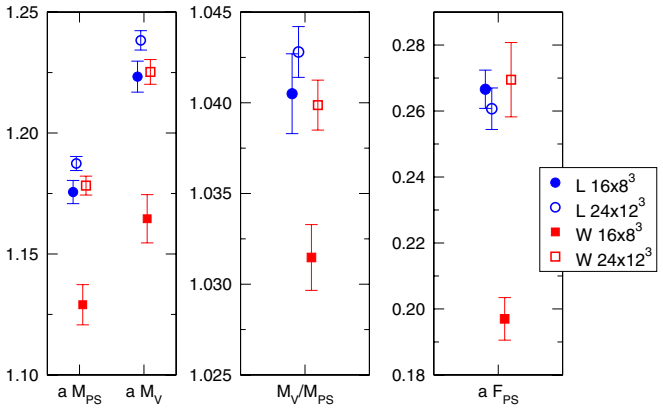

FIG. 17 (color online). PS and V masses, their ratio, and PS decay constant on 16×8^3 and 24×12^3 lattices for $am_0 = -1.05$ and $\beta = 2.25$.

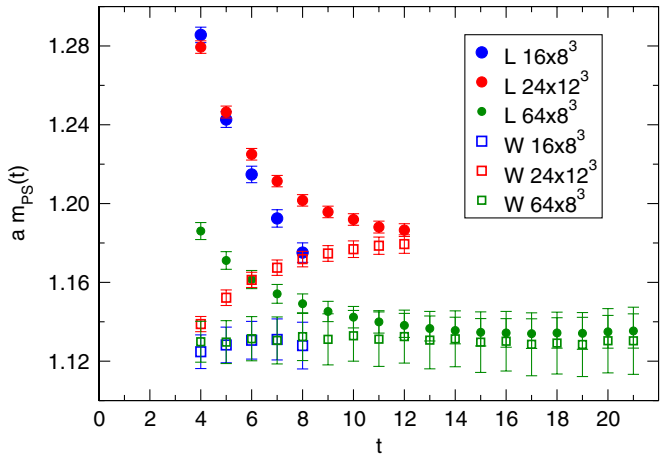

FIG. 18 (color online). Effective PS mass on different volumes for $am_0 = -1.05$ and $\beta = 2.25$. At t larger than 21, this quantity (on the 64×8^3 lattice) becomes much noisier and we cut it for sake of clarity.

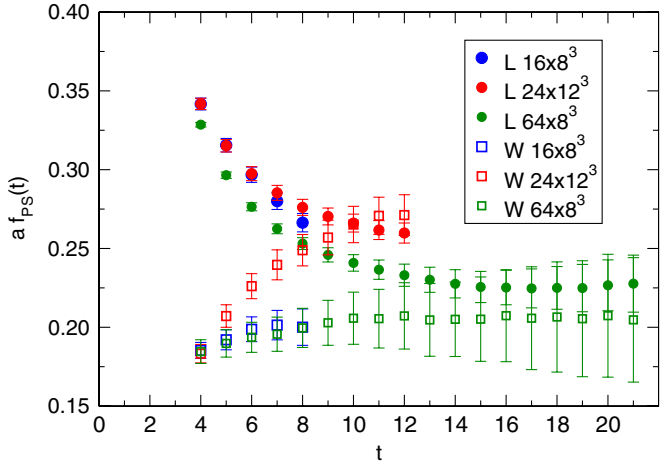

FIG. 19 (color online). Effective PS decay constant on different volumes for $am_0 = -1.05$ and $\beta = 2.25$. At t larger than 21, this quantity (on the 64×8^3 lattice) becomes much noisier and we cut it for the sake of clarity.

effect of making the pseudoscalar meson lighter. What is happening then with the 16×8^3 lattice? The mass estimated with the local sources is affected by two relatively large effects: the finite volume, which decreases the mass and the bad determination of the plateaux, which increases the mass. Having opposite sign and accidentally the same magnitude, these two effects cancel each other. Therefore the finite-volume effects are actually larger than what we estimated on the basis of the local sources, and they are better estimated using the wall-smeared source at light enough masses.

The conclusions above are valid also for the vector meson mass and for the ratio M_V/M_{PS}. In particular from Fig. 11 it is clear that, on increasing the spatial volume, the ratio M_V/M_{PS} slightly increases, and this effect was completely hidden in the local-source determination.

VI. CONCLUSIONS

In this article we have studied systematic effects on the PCAC mass, the mesonic masses, and decay constants due to a short temporal size on the SU(2) gauge theory with two Dirac fermions in the adjoint representation. In order to isolate the ground state in correlators one should take the source and sink infinitely distant. In practice one defines effective quantities (masses and decay constants) which depend on the time separation between source and sink, and which show a plateau at large distances. The value of the plateau gives an estimate for the corresponding mass or decay constant. At fixed temporal extent one can increase the relative amplitude of the ground state in correlators, using smeared sources and/or sinks. This translates into flatter and longer plateaux in the effective quantities.

We have extended the CHROMA suite of software in order to operate with fermions in the adjoint representation of the gauge group, and we have used the CHROMA built-in routines for measuring mesonic correlators with both Gaussian and wall-smeared sources. We observe that at our lightest masses the wall-smearing gives always the best overlap with the ground state. At heavy masses the mesonic wave functions are more localized and the local sources give a better overlap with the ground state. There is an intermediate regime of masses in which the local and wall-smearing sources yield plateaux of similar quality. In this case a Gaussian smearing with properly chosen width might be desirable. If one wants a procedure that enhances the overlap with the ground state at any mass, one should use a variational method with a large set of smeared sources. However, since the interesting physical region is close to the chiral limit, we chose simplicity against generality and we focused our detailed analysis on the wall-smearing only.

The enhancement of the plateaux with smeared sources does not come for free. Observables obtained with smeared sources have longer autocorrelation times. For a fixed set of configurations, a better control on the systematic error

with respect to local sources is generally obtained at the cost of a larger statistical uncertainty.

Among the observables that we have considered, the PCAC mass is the least affected by the systematics, while the decay constants are the most affected. In the region $aM_{\mathrm{PS}} < 0.5$, the 16×8^3 lattice yields relative systematic errors for the PS mass larger than 10%. At least the 24×12^3 lattice is needed in order to stay below 10%.

We also investigated how the finite temporal extent can conspire to partially mask effects due to finite spatial volume, and discovered that finite-volume effects were underestimated in our analysis with local sources. The relative difference between the determinations of the PS mass on the 16×8^3 and 24×12^3 lattices is of order 5% at $aM_{\mathrm{PS}} \simeq 1$ and it goes up to 14% at about $aM_{\mathrm{PS}} \simeq 0.3$. Again, in the interesting region of masses, the 16×8^3 lattice appears to be way too far from the infinite volume limit. A detailed study of finite-volume effects is extremely important in order to address issues like IR conformality, and represents one of our major research lines. This paper represents a clear step forward in a comprehensive study of finite size effects. However, a systematic investigation of the spatial volume dependency of the system is beyond the scope of the present paper and will be presented in a forthcoming work.

Finally, we notice that our conclusions regarding the near-conformal dynamics of this theory are robust, since the main qualitative features already presented in Refs. [22,25] are confirmed by the present analysis.

ACKNOWLEDGMENTS

The numerical calculations presented in this work have been performed on the Horseshoe6 cluster at the University of Southern Denmark (SDU) funded by the Danish Centre for Scientific Computing for the project ''Origin of Mass'' 2009/2010. E. K. is supported by SUPA, the Scottish Universities Physics Alliance. A. R. thanks the Deutsche Forschungsgemeinschaft for financial support. B. L. is supported by the Royal Society. A. P. was supported by the EC (Research Infrastructure Action in FP7, project *HadronPhysics2*). The development of the code used in this work was partially supported by the EPSRC Grant No. EP/F010303/1. We thank the DEISA Consortium (www.deisa.eu), funded through the EU FP7 project RI-222919, for support within the DEISA Extreme Computing Initiative. L. D. D. and B. L. would like to thank the GGI in Florence for hospitality during the final stage of this work.

APPENDIX A: CORRELATORS AND SMEARINGS

1. Local correlators

In order to measure mesonic observables we measure zero-momentum correlators of the form

$$f_{\Gamma\Gamma'}(t) = \sum_{\vec{x}} \langle \mathcal{O}_{\Gamma}^{\mathrm{SINK}\dagger}(\vec{x}, t) \mathcal{O}_{\Gamma'}^{\mathrm{SRCE}}(\vec{0}, 0) \rangle, \tag{A1}$$

where $\mathcal{O}_{\Gamma}^{\mathrm{SRCE,SINK}}$ are interpolating quark bilinear operators with the correct symmetries under spin and parity. We require the isospin nonsinglet correlators and so, for example, we could construct a *local* correlator with the most immediate choice

$$\mathcal{O}_{\Gamma}^{\mathrm{SRCE}}(\vec{x}, t) = \mathcal{O}_{\Gamma}^{\mathrm{SINK}}(\vec{x}, t) = \bar{\psi}_1(\vec{x}, t) \Gamma \psi_2(\vec{x}, t), \tag{A2}$$

where the labels i on the quark fields ψ_i denotes the fermion flavor. Here Γ is a matrix in the Dirac algebra, which determines the symmetries of the operator. This choice reproduces the correlators considered in [25]:

$$f^{\mathrm{L}}_{\Gamma\Gamma'}(t) = \sum_{\vec{x}} \langle (\bar{\psi}_1(\vec{x}, t) \Gamma \psi_2(\vec{x}, t))^{\dagger} \bar{\psi}_1(\vec{0}, 0) \Gamma' \psi_2(\vec{0}, 0) \rangle, \tag{A3}$$

where here the superscript on $f_{\Gamma\Gamma'}$ indicates the local choice. This correlator is measured by computing the quark propagator $S(\vec{x}, t; \vec{x}', t')$, in terms of which

$$f^{\mathrm{L}}_{\Gamma\Gamma'}(t) = -\frac{a^3}{V_s} \sum_{\vec{x}} \mathrm{Tr}[\gamma_0 \Gamma^{\dagger} \gamma_0 S(\vec{x}, t; \vec{0}, 0) \Gamma' \gamma_5 S(\vec{x}, t; \vec{0}, 0)^{\dagger} \gamma_5]. \tag{A4}$$

The propagator is computed by solving the equation

$$a^4 \sum_{\mathbf{y}} D(\mathbf{x}; \mathbf{y}) S(\mathbf{y}, \mathbf{z}) = I \delta_{\mathbf{x};\mathbf{z}}, \tag{A5}$$

where the boldface variables denote the full spacetime coordinate, I denotes the identity matrix in spin and color space, and $D(\mathbf{x}; \mathbf{y})$ is the Dirac matrix.

2. Extended quark fields

In order to obtain an optimum signal for the masses we aim to extract from these correlators, we should construct interpolating operators with a maximized overlap with the desired ground state. The local operators (A2) are not expected to satisfy this requirement well, as the mesons typically have an extension of many times the lattice spacing in a typical simulation. We can improve the situation by considering an operator which is extended spatially over the lattice:

$$\mathcal{O}_{\Gamma}(\vec{x}, t) = \sum_{\vec{y}_1, \vec{y}_2} \Psi(\vec{x}, \vec{y}_1, \vec{y}_2) \bar{\psi}_1(\vec{y}_1, t) \Gamma \psi_2(\vec{y}_2, t). \tag{A6}$$

Usually shell-model wave functions are used [33], meaning the positions of the quark and antiquark are decoupled:

$$\Psi(\vec{x}, \vec{y}_1, \vec{y}_2) = \phi(\vec{x}, \vec{y}_1) \phi(\vec{x}, \vec{y}_2). \tag{A7}$$

The choice $\phi(\vec{x}, \vec{y}) = \delta_{\vec{x},\vec{y}}$ reproduces the point-point case (A2).

In general, such wave functions are not gauge invariant, and as such any expectation value over an ensemble of gauge configurations, in which they are used, must vanish, according to Elitzur's theorem [34]. To avoid this we can fix the gauge on each configuration, being careful to check for errors introduced by the issue of Gribov copies.

Using $\phi^{\mathrm{SRCE/SINK}}$ to define $\mathcal{O}^{\mathrm{SRCE/SINK}}$ we see that our correlation function can be computed as

$$f_{\Gamma\Gamma'}(t) = -\sum_{\vec{x}} \mathrm{Tr}[\gamma_0\Gamma^\dagger\gamma_0\hat{S}(\vec{x}, t; \vec{0}, 0)\Gamma'\gamma_5\hat{S}(\vec{x}, t; \vec{0}, 0)^\dagger\gamma_5], \tag{A8}$$

where $\hat{S}(\vec{x}, t; \vec{x}', t')$ is defined as

$$\hat{S}(\vec{x}, t; \vec{x}', t') = \sum_{\vec{y},\vec{y}'} S(\vec{y}, t; \vec{y}', t')\phi^{\mathrm{SINK}}(\vec{x}, \vec{y})\phi^{\mathrm{SRCE}}(\vec{x}', \vec{y}'). \tag{A9}$$

It can be easily seen that if we solve for S', the system

$$a^4\sum_{\mathbf{y}} D(\mathbf{x}, \mathbf{y})S'(\mathbf{y}, \mathbf{z}) = \phi^{\mathrm{SRCE}}(\vec{z}, \vec{x})\delta_{x_0,z_0}, \tag{A10}$$

we can compute $\hat{S}$ as

$$\hat{S}(\vec{x}, t; \vec{x}', t') = \sum_{\vec{y}} S'(\vec{y}, t; \vec{x}', t')\phi^{\mathrm{SINK}}(\vec{x}, \vec{y}). \tag{A11}$$

In fact it is the choice of a shell-model type wave-function (A7) that allows us to calculate the correlation function using only one inversion of the Dirac matrix (per color and spin index).

3. Smearing examples

A simple guess for an effective form of $\phi(\vec{x})$ is in the form of a Gaussian

$$\phi(\vec{x}, \vec{y}) = e^{-(|\vec{x}-\vec{y}|/R)^2}, \tag{A12}$$

where $R > 0$ is some effective radius chosen to represent the wave function of the meson of interest. The choice $\frac{1}{R} \to 0$ results in $\phi(\vec{x}, \vec{y})$ having equal weight over the whole lattice, and is termed a *wall smearing*.

On a lattice we can approximate the Gaussian as the limit of the iterative form

$$\phi(\vec{x}, \vec{y}) = \left(1 - \frac{w^2}{4N}\Box\right)^N \delta_{\vec{x},\vec{y}}, \tag{A13}$$

where $\Box$ is the lattice version of the Laplacian

$$\Box(\vec{x}, \vec{y}) = \sum_{i=1}^{3}(\delta_{\vec{x},\vec{y}-\hat{i}} + \delta_{\vec{x},\vec{y}+\hat{i}}). \tag{A14}$$

(A13) then approximates (A12) in the limit $N \to \infty$, with the radius R being determined by w. Replacing $\Box$ with its covariant form

$$\Box(\vec{x}, \vec{y}; t) = \sum_{i=1}^{3}(U_i(\vec{x}, t)\delta_{\vec{x},\vec{y}-\hat{i}} + U_i^\dagger(\vec{x} - \hat{i}, t)\delta_{\vec{x},\vec{y}+\hat{i}}), \tag{A15}$$

results in a gauge-invariant operator, negating the requirement for gauge fixing. This choice of ϕ is called *gauge-invariant Gaussian smearing*.

We have utilized both a wall smearing (denoted W) and a gauge-invariant Gaussian smearing (denoted G) in our study.

4. Gauge fixing

When constructing a correlator involving the gauge-dependent wall-smeared quark bilinear, we must fix the gauge on each configuration with which we wish to work. We fix to Coulomb gauge by generating a gauge-fixed gauge configuration from the original by maximizing the quantity $\sum_{\mathbf{x}}\sum_{i=1}^{3} \mathrm{Re}(\mathrm{Tr}[U_i(\mathbf{x})])$.

APPENDIX B: MESON CORRELATOR PHENOMENOLOGY

1. Meson masses

We extract the meson masses from our theory by analyzing correlators of the form (A1) in the case where we consider source and sink operators with equal symmetries, i.e., $\Gamma = \Gamma'$, and so we shall write $f_{\Gamma\Gamma} = f_\Gamma$. We can write f_Γ explicitly as an expectation value on the vacuum state $|0\rangle$:

$$f_\Gamma(t) = \sum_{\vec{x}} \langle 0|\mathcal{O}_\Gamma^{\mathrm{SINK}^\dagger}(\vec{x}, t)\mathcal{O}_\Gamma^{\mathrm{SRCE}}(\vec{0}, 0)|0\rangle. \tag{B1}$$

Labeling the energy eigenstates of the theory as $|n, \vec{p}\rangle$, we can write a complete set of states as

$$\sum_n \int \frac{d^3p}{(2\pi)^3 2E_n(\vec{p})} |n, \vec{p}\rangle\langle n, \vec{p}|. \tag{B2}$$

We can insert this in f_Γ producing

$$f_\Gamma(t) = \sum_n \sum_{\vec{x}} \int \frac{d^3p}{(2\pi)^3 2E_n(\vec{p})} \langle 0|\mathcal{O}_\Gamma^{\mathrm{SINK}^\dagger}(\vec{x}, t)|n, \vec{p}\rangle \times \langle n, \vec{p}|\mathcal{O}_\Gamma^{\mathrm{SRCE}}(\vec{0}, 0)|0\rangle. \tag{B3}$$

Translating $\mathcal{O}^{\mathrm{SINK}}(\mathbf{x})$ to the origin produces $e^{i\mathcal{P}\cdot\mathbf{x}}\mathcal{O}^{\mathrm{SINK}}(\mathbf{0})e^{-i\mathcal{P}\cdot\mathbf{x}}$ where the four-momentum operator $\mathcal{P} = \{\mathcal{H}, \vec{\mathcal{P}}\}$ giving

$$\langle 0|\mathcal{O}_\Gamma^{\mathrm{SINK}^\dagger}(\vec{x}, t)|n, \vec{p}\rangle = \langle 0|\mathcal{O}_\Gamma^{\mathrm{SINK}^\dagger}(\mathbf{0})|n, \vec{p}\rangle e^{-i\mathbf{p}\cdot\mathbf{x}}, \tag{B4}$$

where $\mathbf{p} = \{E_n(\vec{p}), \vec{p}\}$. As a result, the sum over the spatial position $\vec{x}$ collapses the sum onto zero-momentum

$$f_\Gamma(t) = \sum_n \frac{1}{2E_n}\langle 0|\mathcal{O}_\Gamma^{\mathrm{SINK}^\dagger}(\vec{0}, 0)|n\rangle\langle n|\mathcal{O}_\Gamma^{\mathrm{SRCE}}(\vec{0}, 0)|0\rangle e^{-iE_n t}, \tag{B5}$$

where we denote $|n, \vec{0}\rangle$ as $|n\rangle$ and $E_n(\vec{0})$ as E_n. The overlaps $\langle 0|\mathcal{O}(\mathbf{0})|n\rangle$ will vanish for all states except those with the same symmetries as $\mathcal{O}_\Gamma$ and we can see that at large Euclidean time $\tau = it$ the correlator is dominated by the lowest in energy of such states that we denote $|\Gamma\rangle$ with

energy E_Γ which, as we are at zero momentum, equals the mass of the state $E_\Gamma = m_\Gamma$:

$$f_\Gamma(\tau) \overset{\tau\to\infty}{\longrightarrow} \frac{1}{2m_\Gamma}\langle 0|\mathcal{O}_\Gamma^{\mathrm{SINK}\dagger}(\vec{0},0)|\Gamma\rangle\langle\Gamma|\mathcal{O}_\Gamma^{\mathrm{SRCE}}(\vec{0},0)|0\rangle e^{-m_\Gamma\tau} \equiv A_\Gamma e^{-m_\Gamma\tau}. \tag{B6}$$

On a lattice with finite temporal extent $0 < \tau < L_t$, this asymptotic behavior is modified by the appearance of an extra term corresponding to a quark propagating backward from source to sink through the antiperiodic boundary:

$$f_\Gamma(\tau) \to A_\Gamma(e^{-m_\Gamma\tau} + e^{-m_\Gamma(L_t-\tau)}) \equiv A_\Gamma hc(\tau, m_\Gamma, L_t). \tag{B7}$$

In this way we can extract the meson masses from the exponential behavior of the f_Γ at large Euclidean time.

As in [25], we use the Prony method [35] to solve this system, to produce an "effective mass" $m_\Gamma(\tau)$ which, as a function of the lattice temporal coordinate, is expected to approach the desired mass in the limit of large times $m_\Gamma(t) \longrightarrow^{\tau\to\infty} m_\Gamma$. The meson mass is extracted by choosing a region around the center of the temporal axis and fitting the effective mass to a constant in this region.

In our study we have considered the case $\Gamma = \gamma_5$, defining the *pseudoscalar* channel, with mass m_{PS} and the degerate cases $\Gamma = \gamma_i \;\; i \in \{1,2,3\}$, defining the *vector* channel with mass m_{V}. In practice the correlators f_{γ_i} are averaged to produce a single correlator for the vector channel. We call the resulting vector correlator f_{VV} and the pseudoscalar correlator f_{PP}.

The masses can be extracted identically from these correlators regardless of the smearing used. In practice it is found that correlators with a smeared source are preferred to local correlators for this purpose, in that they produce an improved signal to noise ratio for the masses. Correlators with smearing at both the source and sink are found to be disfavored because of enhanced fluctuations.

2. Amplitudes

If local quark fields are used, $\mathcal{O}_\Gamma^{\mathrm{SRCE/SINK}}(\mathbf{x}) = \bar{\psi}_1(\mathbf{x})\Gamma\psi_2(\mathbf{x}) = \mathcal{O}_\Gamma^{\mathrm{L}}(\mathbf{x})$. In the case of both the pseudoscalar and vector channels, we are interested in the quantity $|\langle 0|\mathcal{O}_\Gamma^{\mathrm{L}}(\mathbf{0})|\Gamma\rangle|$ although they have different meanings:

$$|\langle 0|\mathcal{O}_{\gamma_5}^{\mathrm{L}}(\mathbf{0})|\gamma_5\rangle| \equiv G_{\mathrm{PS}}, \qquad |\langle 0|\mathcal{O}_{\gamma_i}^{\mathrm{L}}(\mathbf{0})|\gamma_i\rangle| \equiv \epsilon_i F_{\mathrm{V}} m_{\mathrm{V}}, \tag{B8}$$

where ϵ_i is a polarization tensor. We call G_{PS} the *psuedoscalar vacuum to meson amplitude* (or, more commonly, simply the psuedoscalar amplitude), and F_{V} is the *vector decay constant*. We can easily construct effective observables for these quantities from the local correlators $f_{\mathrm{PP}}^{\mathrm{L}}$ and $f_{\mathrm{VV}}^{\mathrm{L}}$:

$$G_{\mathrm{PS}}^{\mathrm{L}}(\tau) = \sqrt{\frac{2m_{\mathrm{PS}}(\tau) f_{\mathrm{PP}}^{\mathrm{L}}(\tau)}{hc(\tau, m_{\mathrm{PS}}(\tau), L_t)}},$$
$$F_{\mathrm{V}}^{\mathrm{L}}(\tau) = \sqrt{\frac{2f_{\mathrm{VV}}^{\mathrm{L}}(\tau)}{m_{\mathrm{V}} hc(\tau, m_{\mathrm{V}}(\tau), L_t)}}. \tag{B9}$$

If we wish to use smeared operators to extract these quantities, the amplitudes in (B6) are, in general, no longer related to the quantities of interest (B8). However, if our correlator involves only a smearing at the source, with a local sink, we see that the sink amplitude in (B6) is still of the correct form (B8). We need cancel the other undesired amplitude introduced by the smearing. We can do this by combining our local-smeared correlator (f_Γ^{LS}) with a smeared-smeared correlator (f_Γ^{SS}). Effective observables equivalent to (B8) can be defined from smeared correlators as

$$G_{\mathrm{PS}}^{S}(\tau) = \sqrt{\frac{2m_{\mathrm{PS}}(\tau)}{hc(\tau, m_{\mathrm{PS}}(\tau), L_t)} \frac{f_{\mathrm{PP}}^{\mathrm{LS}^2}(\tau)}{f_{\mathrm{PP}}^{\mathrm{SS}}(\tau)}},$$
$$F_{\mathrm{V}}^{S}(\tau) = \sqrt{\frac{2}{m_{\mathrm{V}} hc(\tau, m_{\mathrm{V}}(\tau), L_t)} \frac{f_{\mathrm{VV}}^{\mathrm{LS}^2}(\tau)}{f_{\mathrm{VV}}^{\mathrm{SS}}(\tau)}}. \tag{B10}$$

3. Quark mass

As our simulation is based on the Wilson quark formulation, the physical quark mass in our simulation m is related to the bare quark mass which is an input to the simulation m_0 by an additive renormalization, which, being a nonperturbative quantity, ca not be calculated *a priori*. As such we must have a method of determining the physical quark mass in the simulation in order to determine our proximity to the chiral point $m = 0$ and to observe the scaling of mesonic observables with m.

The most straightforward such method is via the *partially conserved axial current mass* or PCAC mass. We define the continuum nonsinglet axial and pseudoscalar currents as

$$A_\mu(\mathbf{x}) = \bar{\psi}_1(\mathbf{x})\gamma_\mu\gamma_5\psi_2(\mathbf{x}), \qquad P(\mathbf{x}) = \bar{\psi}_1(\mathbf{x})\gamma_5\psi_2(\mathbf{x}). \tag{B11}$$

We see that these are continuum versions of our $\mathcal{O}_{\gamma_\mu\gamma_5}^{\mathrm{L}}$ and $\mathcal{O}_{\gamma_5}^{\mathrm{L}}$. From the Ward identity for the axial transformation $\psi \to e^{i\alpha\gamma_5}\psi$ we obtain for the divergence of the axial current

$$\partial_\mu A_\mu(\mathbf{x}) = -2mP(\mathbf{x}), \tag{B12}$$

where m is the physical quark mass, as above. From this we obtain

$$\frac{\partial}{\partial t}\int d^3x\langle A_0(\vec{x},t)\mathcal{O}_{\gamma_5}\rangle = -2m\langle P(\vec{x},t)\mathcal{O}_{\gamma_5}\rangle, \tag{B13}$$

where $\mathcal{O}_{\gamma_5}$ is any bilinear quark operator with the symmetries of a pseudoscalar current. Taking a lattice version of this, and choosing for $\mathcal{O}_{\gamma_5}$ any of the local or smeared lattice pseudoscalar currents we have previously constructed, we see we can define an effective PCAC quark mass via

$$m(\tau) = \frac{m_{\mathrm{PS}}}{\sinh(am_{\mathrm{PS}})} \frac{f^{\mathrm{LS}}_{\mathrm{AP}}(\tau - a) - f^{\mathrm{LS}}_{\mathrm{AP}}(\tau + a)}{4f^{\mathrm{LS}}_{\mathrm{PP}}(\tau)}, \quad \text{(B14)}$$

where we define f_{AP} to be $f_{\gamma_0\gamma_5,\gamma_5}$. The prefactor of $\frac{m_{\mathrm{PS}}}{\sinh(am_{\mathrm{PS}})}$ arises by a choice of the lattice finite difference operator which more accurately represents the continuum derivative on f_{AP}. The correlators f^{LS} are constructed with a local sink, and a source which can be local, or involve any smearing.

4. Pseudoscalar decay constant

Similarly to (B6) the correlator f_{AP} has an asymptotic behavior:

$$f_{\mathrm{AP}}(\tau) \xrightarrow{\tau\to\infty} \frac{1}{2m_{\mathrm{PS}}} \langle 0|\mathcal{O}^{\mathrm{SINK}\dagger}_{\gamma_0\gamma_5}(\vec{0},0)|\gamma_5\rangle\langle\gamma_5|\mathcal{O}^{\mathrm{SRCE}}_{\gamma_5}(\vec{0},0)|0\rangle e^{-m_{\mathrm{PS}}\tau} \equiv A_{\mathrm{AP}} e^{-m_{\mathrm{PS}}\tau}. \quad \text{(B15)}$$

In contrast to (B7) however, the contribution to f_{AP} from propagation around the lattice comes with the opposite sign, so on a lattice with finite temporal extent,

$$f_{\mathrm{AP}}(\tau) \to A_{\mathrm{AP}}(e^{-m_{\mathrm{PS}}\tau} - e^{-m_{\mathrm{PS}}(L_t-\tau)}) \equiv A_{\mathrm{AP}} hs(\tau, m_{\mathrm{PS}}, L_t). \quad \text{(B16)}$$

Now we define the *pseudoscalar decay constant* F_{PS} as

$$m_{\mathrm{PS}} F_{\mathrm{PS}} = \langle 0|\mathcal{O}^{\mathrm{L}}_{\gamma_0\gamma_5}(\vec{0},0)|\gamma_5\rangle. \quad \text{(B17)}$$

Combining this with the Ward identity for f_{AP} we can define an effective observable for F_{PS} as

$$F^{S}_{\mathrm{PS}}(\tau) = \frac{2m(\tau)G^{S}_{\mathrm{PS}}(\tau)}{m^2_{\mathrm{PS}}(\tau)}. \quad \text{(B18)}$$

The superscript S here indicates that this is valid for observables obtained from any smeared correlator, provided the corresponding definition of G_{PS} is used, from (B9) or (B10).

C. RESULTS TABLES

TABLE I. Results for mesonic observables from wall-smeared correlators on a 16×8^3 lattice at $\beta = 2.25$.

Lattice	$-am_0$	N_{conf}	am	am_{PS}	am_{V}	aF_{PS}	aF_{V}
S0	−0.5	901	1.163 53(73)	2.7983(15)	2.8042(16)	0.2950(73)	0.3338(92)
S1	−0.25	901	1.072 05(97)	2.6535(21)	2.6613(22)	0.3150(63)	0.3629(80)
S2	0	901	0.9706(11)	2.4938(25)	2.5045(27)	0.3335(63)	0.3935(84)
S3	0.25	901	0.8552(11)	2.3092(28)	2.3241(31)	0.3579(74)	0.435(10)
S4	0.5	901	0.7224(13)	2.0934(32)	2.1155(37)	0.3729(87)	0.475(13)
S5	0.75	901	0.5607(18)	1.8136(47)	1.8473(55)	0.375(12)	0.511(21)
S6	0.9	901	0.4330(18)	1.5582(68)	1.5987(81)	0.315(13)	0.441(23)
A0	0.95	1501	0.3849(16)	1.4488(68)	1.4902(84)	0.291(12)	0.411(22)
A1	0.975	1499	0.3582(17)	1.3830(74)	1.4251(91)	0.274(11)	0.388(21)
A2	1	7300	0.3314(19)	1.3137(78)	1.3553(97)	0.258(13)	0.368(23)
A3	1.025	1481	0.3001(19)	1.2222(90)	1.260(11)	0.230(10)	0.324(18)
A4	1.05	1481	0.2688(15)	1.1290(83)	1.1645(99)	0.1970(64)	0.2692(89)
A5	1.075	1277	0.2352(18)	1.011(13)	1.042(16)	0.185(11)	0.258(20)
A6	1.1	1279	0.1992(32)	0.886(14)	0.914(19)	0.1642(99)	0.227(17)
A7	1.125	1344	0.1595(25)	0.725(14)	0.747(18)	0.1478(76)	0.200(15)
A8	1.15	1278	0.1150(31)	0.519(18)	0.534(23)	0.1439(70)	0.194(10)
A9	1.175	1280	0.0628(30)	0.285(23)	0.295(30)	0.1569(43)	0.2120(81)

TABLE II. Results for mesonic observables from wall-smeared correlators on a 24×12^3 lattice at $\beta = 2.25$.

Lattice	$-am_0$	N_{conf}	am	am_{PS}	am_{V}	aF_{PS}	aF_{V}
B0	0.95	1973	0.390 17(68)	1.4720(23)	1.5186(28)	0.3220(61)	0.468(11)
B1	1	1689	0.336 23(82)	1.3441(28)	1.3932(37)	0.2942(73)	0.434(13)
B2	1.05	1564	0.274 70(91)	1.1782(39)	1.2252(51)	0.269(11)	0.395(19)
B3	1.075	1438	0.2393(10)	1.0660(55)	1.1058(68)	0.231(13)	0.333(24)
B4	1.1	5112	0.2014(10)	0.9310(65)	0.9638(79)	0.1523(85)	0.208(14)
B5	1.125	1240	0.160 13(92)	0.7697(60)	0.7963(68)	0.1485(63)	0.2062(97)
B6	1.15	640	0.1149(15)	0.572(12)	0.588(15)	0.0955(53)	0.1296(89)
B7	1.175	5137	0.0653(14)	0.3277(95)	0.336(11)	0.0985(33)	0.1298(54)
B8	1.18	818	0.0547(17)	0.282(11)	0.294(13)	0.0984(53)	0.1311(78)
B9	1.185	840	0.0418(16)	0.206(11)	0.213(11)	0.1056(43)	0.1366(63)
B10	1.19	700	0.0300(11)	0.1476(82)	0.1539(96)	0.1129(32)	0.1496(36)

TABLE III. Results for mesonic observables from wall-smeared correlators on a 32×16^3 lattice at $\beta = 2.25$.

Lattice	$-am_0$	N_{conf}	am	am_{PS}	am_{V}	aF_{PS}	aF_{V}
C0	1.15	1090	0.117 31(77)	0.6121(64)	0.6305(83)	0.0983(44)	0.1314(87)
C1	1.175	523	0.065 79(77)	0.3652(87)	0.381(10)	0.0746(35)	0.1037(64)
C2	1.18	917	0.054 37(79)	0.3042(69)	0.3174(80)	0.0736(37)	0.0992(59)
C3	1.185	864	0.042 17(84)	0.2241(62)	0.2297(72)	0.0763(32)	0.0992(44)
C4	1.19	1083	0.030 65(72)	0.1682(62)	0.1764(64)	0.0776(27)	0.1038(36)

TABLE IV. Results for mesonic observables from wall-smeared correlators on a 64×24^3 lattice at $\beta = 2.25$.

Lattice	$-am_0$	N_{conf}	am	am_{PS}	am_{V}	aF_{PS}	aF_{V}
D0	1.18	185	0.055 28(25)	0.3239(49)	0.3295(62)	0.0398(27)	0.0455(41)
D1	1.185	164	0.042 87(29)	0.2462(58)	0.2566(75)	0.0696(65)	0.091(11)
D2	1.19	160	0.029 67(50)	0.1741(52)	0.1759(59)	0.0501(30)	0.0601(52)

TABLE V. Results for mesonic observables from wall-smeared correlators on a 64×24^3 lattice at $\beta = 2.1$.

Lattice	$-am_0$	N_{conf}	am	am_{PS}	am_{V}	aF_{PS}	aF_{V}
E0	1.25	131	0.117 51(28)	0.7173(11)	0.7735(39)	0.1592(26)	0.263(12)
E1	1.26	130	0.085 27(34)	0.5612(15)	0.5881(45)	0.1122(26)	0.169(11)

TABLE VI. Ratios of mesonic observables from wall-smeared correlators on a 16×8^3 lattice at $\beta = 2.25$.

Lattice	$-am_0$	am_{PS}^2/m	m_V/F_{PS}	m_V/m_{PS}	$a^3(m_{PS}F_{PS})^2/m$	F_V/F_{PS}
S0	−0.5	6.7300(39)	9.50(23)	1.002 100(47)	0.586(29)	1.1311(35)
S1	−0.25	6.5681(57)	8.45(16)	1.002 94(10)	0.652(26)	1.1520(29)
S2	0	6.4070(67)	7.51(13)	1.004 28(14)	0.713(27)	1.1797(37)
S3	0.25	6.2347(86)	6.49(13)	1.006 47(22)	0.798(33)	1.2172(50)
S4	0.5	6.065(10)	5.67(12)	1.010 58(36)	0.844(40)	1.2754(72)
S5	0.75	5.866(17)	4.91(16)	1.018 58(75)	0.830(57)	1.359(14)
S6	0.9	5.606(31)	5.07(19)	1.0259(11)	0.558(49)	1.398(18)
A0	0.95	5.453(33)	5.11(19)	1.0286(13)	0.465(41)	1.408(19)
A1	0.975	5.338(37)	5.20(20)	1.0303(15)	0.402(37)	1.414(18)
A2	1	5.206(40)	5.24(24)	1.0316(17)	0.350(36)	1.421(24)
A3	1.025	4.977(47)	5.47(22)	1.0308(19)	0.265(26)	1.405(21)
A4	1.05	4.741(48)	5.91(16)	1.0314(18)	0.184(13)	1.366(18)
A5	1.075	4.352(94)	5.63(29)	1.0300(50)	0.150(21)	1.390(32)
A6	1.1	3.94(10)	5.58(27)	1.0310(70)	0.107(14)	1.385(37)
A7	1.125	3.299(93)	5.06(20)	1.0307(70)	0.0724(87)	1.358(54)
A8	1.15	2.35(13)	3.71(17)	1.028(16)	0.0489(60)	1.350(31)
A9	1.175	1.30(19)	1.88(20)	1.034(44)	0.0320(48)	1.351(39)

TABLE VII. Ratios of mesonic observables from wall-smeared correlators on a 24×12^3 lattice at $\beta = 2.25$.

Lattice	$-am_0$	am_{PS}^2/m	m_V/F_{PS}	m_V/m_{PS}	$a^3(m_{PS}F_{PS})^2/m$	F_V/F_{PS}
B0	0.95	5.553(10)	4.717(84)	1.03166(59)	0.576(22)	1.454(12)
B1	1	5.373(13)	4.73(11)	1.03652(96)	0.465(23)	1.476(20)
B2	1.05	5.053(21)	4.55(17)	1.0398(13)	0.367(31)	1.465(19)
B3	1.075	4.748(35)	4.79(26)	1.0373(21)	0.255(30)	1.438(31)
B4	1.1	4.303(42)	6.34(32)	1.0352(18)	0.100(11)	1.365(27)
B5	1.125	3.700(42)	5.36(20)	1.0345(18)	0.0818(77)	1.388(14)
B6	1.15	2.84(10)	6.17(26)	1.0287(85)	0.0261(35)	1.355(38)
B7	1.175	1.644(71)	3.41(12)	1.026(12)	0.0160(14)	1.317(25)
B8	1.18	1.457(93)	2.99(19)	1.042(21)	0.0141(18)	1.332(30)
B9	1.185	1.022(90)	2.02(12)	1.034(23)	0.0114(12)	1.293(44)
B10	1.19	0.727(68)	1.36(10)	1.043(32)	0.00926(75)	1.325(37)

TABLE VIII. Ratios of mesonic observables from wall-smeared correlators on a 32×16^3 lattice at $\beta = 2.25$.

Lattice	$-am_0$	am_{PS}^2/m	m_V/F_{PS}	m_V/m_{PS}	$a^3(m_{PS}F_{PS})^2/m$	F_V/F_{PS}
C0	1.15	3.194(53)	6.41(25)	1.0299(47)	0.0310(30)	1.334(40)
C1	1.175	2.028(87)	5.12(21)	1.045(10)	0.0113(14)	1.389(37)
C2	1.18	1.702(62)	4.32(20)	1.043(10)	0.0092(10)	1.348(28)
C3	1.185	1.191(55)	3.01(13)	1.024(16)	0.006 96(68)	1.298(23)
C4	1.19	0.924(57)	2.27(11)	1.048(20)	0.005 57(46)	1.336(26)

TABLE IX. Ratios of mesonic observables from wall-smeared correlators on a 64×24^3 lattice at $\beta = 2.25$.

Lattice	$-am_0$	am_{PS}^2/m	m_V/F_{PS}	m_V/m_{PS}	$a^3(m_{PS}F_{PS})^2/m$	F_V/F_{PS}
D0	1.18	1.899(55)	8.29(45)	1.0169(88)	0.003 04(51)	1.140(47)
D1	1.185	1.414(64)	3.70(28)	1.042(14)	0.0069(15)	1.308(59)
D2	1.19	1.023(53)	3.51(17)	1.009(19)	0.002 59(42)	1.199(54)

TABLE X. Ratios of mesonic observables from wall-smeared correlators on a 64×24^3 lattice at $\beta = 2.1$.

Lattice	$-am_0$	am_{PS}^2/m	m_V/F_{PS}	m_V/m_{PS}	$a^3(m_{PS}F_{PS})^2/m$	F_V/F_{PS}
E0	1.25	4.378(10)	4.857(81)	1.0783(49)	0.1110(37)	1.653(76)
E1	1.26	3.693(21)	5.24(12)	1.0479(79)	0.0465(22)	1.50(10)

D. PULL TABLES

TABLE XI. Pull of wall-smeared results from local results on a 16×8^3 lattice.

Lattice	V	$-am_0$	am	am_{PS}	a^2G_{PS}	aF_{PS}	am_V	aF_V
S0	16×8^3	−0.5	0.357 743	0.630 827	0.235 108	0.256 243	0.620 554	0.183 502
S1	16×8^3	−0.25	0.089 053 5	0.370 89	0.250 73	0.185 906	0.364 952	0.221 968
S2	16×8^3	0	0.176 656	0.103 129	0.633 081	0.570 268	0.117 478	0.603 322
S3	16×8^3	0.25	0.054 422 1	0.891 48	0.546 006	0.402 862	0.863 709	0.524 572
S4	16×8^3	0.5	0.412 61	0.213 066	0.745 81	0.769 548	0.198 067	0.685 742
S5	16×8^3	0.75	0.798 726	0.721 695	0.723 448	0.773 543	0.764 52	0.658 796
S6	16×8^3	0.9	0.914 745	2.123 96	2.852 72	2.626 16	2.197 36	2.969 89
A0	16×8^3	0.95	1.170 47	2.877 97	3.536 52	3.173 06	3.0289	3.705 67
A1	16×8^3	0.975	1.482 67	3.037 48	3.0976	3.696 49	3.1175	4.284 69
A2	16×8^3	1	1.085 58	3.307 53	3.8366	3.396 84	3.389 91	3.995 93
A3	16×8^3	1.025	1.504 36	4.027 95	5.567 33	4.938 76	4.087 13	5.906 23
A4	16×8^3	1.05	1.447 32	4.8367	9.425 37	8.005 32	4.942 94	12.0426
A5	16×8^3	1.075	0.854 806	3.471 75	6.880 26	4.079 07	3.406 87	5.065 41
A6	16×8^3	1.1	0.761 814	3.250 19	5.457 58	4.427 01	3.037 32	5.346 94
A7	16×8^3	1.125	1.073 67	3.4146	5.774 55	4.517 91	3.050 06	4.975 78
A8	16×8^3	1.15	0.769 772	2.642 52	3.779 74	2.612 07	2.056 69	3.824 54
A9	16×8^3	1.175	0.567 182	1.702 04	1.912 51	0.632 631	1.611 41	2.250 52

TABLE XII. Pull of wall-smeared results from local results on a 24×12^3 lattice.

Lattice	V	$-am_0$	am	am_{PS}	a^2G_{PS}	aF_{PS}	am_V	aF_V
B0	24×12^3	0.95	0.774 467	0.783 603	1.423 61	1.408 95	0.8713 24	1.537 57
B1	24×12^3	1	0.159 875	1.401 15	1.183 23	0.807 577	1.360 64	1.469 37
B2	24×12^3	1.05	0.457 775	1.859 51	0.417 244	0.680 213	2.013 02	0.207 503
B3	24×12^3	1.075	0.431 929	2.359 26	0.376 053	0.036 731 3	2.574 14	0.556 833
B4	24×12^3	1.1	0.273 78	4.084 46	5.1113	4.655 01	4.100 09	5.441 29
B5	24×12^3	1.125	0.092 912 3	4.425 96	3.326 75	1.769 42	3.942 36	2.575 02
B6	24×12^3	1.15	0.886 415	2.496 18	4.857 51	3.772 26	2.044 29	3.868 22
B7	24×12^3	1.175	0.252 409	2.908 99	3.776 84	1.8568	2.293 01	2.326 82
B8	24×12^3	1.18	0.623 981	1.973 81	2.989 03	1.748 13	1.6552	2.725 08
B9	24×12^3	1.185	0.455 37	1.691 78	2.276 98	0.544 327	0.994 413	2.105 43
B10	24×12^3	1.19	0.107 576	1.616 24	1.861 86	0.8264	0.831 428	1.556 31

TABLE XIII. Pull of wall-smeared results from local results on a 32×16^3 lattice.

Lattice	V	$-am_0$	am	am_{PS}	a^2G_{PS}	aF_{PS}	am_V	aF_V
C0	32×16^3	1.15	0.082 699 8	2.765 28	4.432 89	3.498 37	2.510 94	3.698 38
C1	32×16^3	1.175	0.656 922	1.804 44	3.885 21	2.7899	1.636 12	3.349 12
C2	32×16^3	1.18	0.297 786	2.346 19	3.686 42	2.424 67	2.038 04	3.610 78
C3	32×16^3	1.185	0.067 722 6	2.363 42	2.478 07	0.443 416	1.667 51	1.681 51
C4	32×16^3	1.19	0.136 12	2.190 63	3.100 32	0.7232	1.754 68	2.793 63

TABLE XIV. Pull of wall-smeared results from local results on a 64×24^3 lattice.

Lattice	V	$-am_0$	am	am_{PS}	a^2G_{PS}	aF_{PS}	am_{V}	aF_{V}
D0	64×24^3	1.18	0.231 276	1.684 37	10.7124	3.654 89	1.980 21	2.999 79
D1	64×24^3	1.185	0.753 454	0.491 626	8.317 95	2.830 08	0.281 183	1.973 54
D2	64×24^3	1.19	0.302 909	0.037 698 7	10.0776	0.153 963	0.124 777	0.183 138

TABLE XV. Pull of wall-smeared results from local results on a 16×8^3 lattice.

Lattice	V	$-am_0$	am_{PS}^2/m	$m_{\mathrm{V}}/F_{\mathrm{PS}}$	$m_{\mathrm{V}}/m_{\mathrm{PS}}$	$a^3(m_{\mathrm{PS}}F_{\mathrm{PS}})^2/m$	$F_{\mathrm{V}}/F_{\mathrm{PS}}$
S0	16×8^3	-0.5	579.839	103.336	42.4374	14.8134	29.6658
S1	16×8^3	-0.25	355.964	115.643	28.3108	17.5745	40.2534
S2	16×8^3	0	256.472	102.845	27.2575	17.0714	36.0592
S3	16×8^3	0.25	161.5	76.8603	27.1434	13.7659	30.298
S4	16×8^3	0.5	105.789	55.6038	25.8027	10.1067	25.9244
S5	16×8^3	0.75	67.0073	41.9002	22.8086	6.02327	18.2194
S6	16×8^3	0.9	162.403	326	21.9192	10.0395	20.4498
A0	16×8^3	0.95	42.936	27.5523	19.6178	1.61548	14.8302
A1	16×8^3	0.975	34.6138	20.3632	18.5986	5.082 23	15.0627
A2	16×8^3	1	29.2933	12.2385	15.9358	7.946 12	10.4417
A3	16×8^3	1.025	27.2297	8.32147	13.3442	16.2042	10.4521
A4	16×8^3	1.05	27.2413	2.958 47	13.634	32.67	7.681 35
A5	16×8^3	1.075	16.7288	0.223 305	3.820 08	26.723	3.435 54
A6	16×8^3	1.1	16.2186	2.762 73	1.6808	24.4004	0.595 224
A7	16×8^3	1.125	19.8065	2.299 41	0.273 288	21.8378	1.642 39
A8	16×8^3	1.15	21.8515	4.29543	0.285 916	27.8008	3.788 25
A9	16×8^3	1.175	20.4856	11.9002	0.005 403 29	27.7572	3.35479

TABLE XVI. Pull of wall-smeared results from local results on a 24×12^3 lattice.

Lattice	V	$-am_0$	am_{PS}^2/m	$m_{\mathrm{V}}/F_{\mathrm{PS}}$	$m_{\mathrm{V}}/m_{\mathrm{PS}}$	$a^3(m_{\mathrm{PS}}F_{\mathrm{PS}})^2/m$	$F_{\mathrm{V}}/F_{\mathrm{PS}}$
B0	24×12^3	0.95	0.396 346	1.386 81	0.717 94	1.400 66	0.622 82
B1	24×12^3	1	0.495 822	0.681 721	0.7434	0.948 186	1.251 64
B2	24×12^3	1.05	0.562 277	0.944 498	1.535 68	0.612 448	2.129 25
B3	24×12^3	1.075	1.167 16	0.223 536	1.730 31	0.172 471	1.358 59
B4	24×12^3	1.1	2.543 33	3.710 56	2.364 72	5.766 23	2.854 06
B5	24×12^3	1.125	3.114 13	1.036 24	0.533 927	2.646 76	1.600 02
B6	24×12^3	1.15	1.510 09	3.610 68	0.122 117	4.287 13	0.420 703
B7	24×12^3	1.175	3.053 79	0.169 209	0.492 669	3.590 39	0.854 043
B8	24×12^3	1.18	1.845 39	0.456 036	0.226 258	2.9395	1.209 18
B9	24×12^3	1.185	1.718 52	0.384 545	1.350 89	1.918 35	1.489 33
B10	24×12^3	1.19	1.742 55	1.0647	0.897 999	1.214 23	1.908 16

TABLE XVII. Pull of wall-smeared results from local results on a 32×16^3 lattice.

Lattice	V	$-am_0$	am_{PS}^2/m	$m_{\mathrm{V}}/F_{\mathrm{PS}}$	$m_{\mathrm{V}}/m_{\mathrm{PS}}$	$a^3(m_{\mathrm{PS}}F_{\mathrm{PS}})^2/m$	$F_{\mathrm{V}}/F_{\mathrm{PS}}$
C0	32×16^3	1.15	1.931 71	3.068 61	0.882 135	4.343 96	1.473 96
C1	32×16^3	1.175	1.064 68	2.325 32	0.137 237	3.318 04	0.411 924
C2	32×16^3	1.18	2.036 76	1.546 44	0.0619 247	3.396 86	1.573 62
C3	32×16^3	1.185	2.396 44	0.563 872	0.653 246	1.823 22	1.421 52
C4	32×16^3	1.19	2.261 97	0.559 476	0.623 971	2.590 77	1.876 11

TABLE XVIII. Pull of wall-smeared results from local results on a 64×24^3 lattice.

Lattice	V	$-am_0$	am_{PS}^2/m	m_V/F_{PS}	m_V/m_{PS}	$a^3(m_{PS}F_{PS})^2/m$	F_V/F_{PS}
D0	64×24^3	1.18	2.045 15	3.803 98	1.327 66	3.075 95	1.800 12
D1	64×24^3	1.185	0.739 296	3.8496	0.192 169	2.020 15	0.046 830 5
D2	64×24^3	1.19	0.139 092	0.267 849	0.156 939	0.100 296	0.348 643

[1] S. Weinberg, Phys. Rev. D **13**, 974 (1976).
[2] L. Susskind, Phys. Rev. D **20**, 2619 (1979).
[3] B. Holdom, Phys. Lett. **150B**, 301 (1985).
[4] K. Yamawaki, M. Bando, and K.-i. Matumoto, Phys. Rev. Lett. **56**, 1335 (1986).
[5] T. W. Appelquist, D. Karabali, and L. C. R. Wijewardhana, Phys. Rev. Lett. **57**, 957 (1986).
[6] M. A. Luty and T. Okui, J. High Energy Phys. 09 (2006) 070.
[7] C. T. Hill and E. H. Simmons, Phys. Rep. **381**, 235 (2003).
[8] F. Sannino, Acta Phys. Pol. B **40**, 3533 (2009).
[9] M. Piai, Adv. High Energy Phys. **2010**, 464302 (2010).
[10] C. Nunez, I. Papadimitriou, and M. Piai, Int. J. Mod. Phys. A **25**, 2837 (2010).
[11] D. Elander, C. Nunez, and M. Piai, Phys. Lett. B **686**, 64 (2010).
[12] T. DeGrand, arXiv:1010.4741.
[13] L. Del Debbio, Proc. Sci., LATTICE2010 (2010) 004.
[14] D. D. Dietrich and F. Sannino, Phys. Rev. D **75**, 085018 (2007).
[15] A. J. Hietanen, K. Rummukainen, and K. Tuominen, Phys. Rev. D **80**, 094504 (2009).
[16] F. Bursa, L. Del Debbio, L. Keegan, C. Pica, and T. Pickup, Phys. Rev. D **81**, 014505 (2010).
[17] T. DeGrand, Y. Shamir, and B. Svetitsky, Phys. Rev. D **83**, 074507 (2011).
[18] S. Catterall and F. Sannino, Phys. Rev. D **76**, 034504 (2007).
[19] L. Del Debbio, A. Patella, and C. Pica, Phys. Rev. D **81**, 094503 (2010).
[20] S. Catterall, J. Giedt, F. Sannino, and J. Schneible, J. High Energy Phys. 11 (2008) 009.
[21] A. Hietanen, J. Rantaharju, K. Rummukainen, and K. Tuominen, Nucl. Phys. **A820**, 191c (2009).
[22] L. Del Debbio, B. Lucini, A. Patella, C. Pica, and A. Rago, Phys. Rev. D **80**, 074507 (2009).
[23] S. Catterall, J. Giedt, F. Sannino, and J. Schneible, arXiv:0910.4387.
[24] L. Del Debbio, B. Lucini, A. Patella, C. Pica, and A. Rago, Phys. Rev. D **82**, 014510 (2010).
[25] L. Del Debbio, B. Lucini, A. Patella, C. Pica, and A. Rago, Phys. Rev. D **82**, 014509 (2010).
[26] T. DeGrand and A. Hasenfratz, Phys. Rev. D **80**, 034506 (2009).
[27] B. Lucini, Phil. Trans. R. Soc. A **368**, 3657 (2010).
[28] L. Del Debbio and R. Zwicky, Phys. Lett. B **700**, 217 (2011).
[29] L. Del Debbio and R. Zwicky, Phys. Rev. D **82**, 014502 (2010).
[30] E. Kerrane *et al.*, Proc. Sci. LATTICE2010 (2010) 058arXiv:1011.0607.
[31] R. G. Edwards and B. Joo (SciDAC Collaboration, LHPC Collaboration, and UKQCD Collaboration Collaboration), Nucl. Phys. B, Proc. Suppl. **140**, 832 (2005).
[32] N. Madras and A. D. Sokal, J. Stat. Phys. **50**, 109 (1988).
[33] T. A. DeGrand and R. D. Loft, Comput. Phys. Commun. **65**, 84 (1991).
[34] S. Elitzur, Phys. Rev. D **12**, 3978 (1975).
[35] G. T. Fleming, S. D. Cohen, H.-W. Lin, and V. Pereyra, Phys. Rev. D **80**, 074506 (2009).